A low-cost small-size commercial PIN photodiode: II. Comparison of measurements with monoenergetic electrons to analytical expressions and Monte Carlo simulations

A. Mangiarotti [a,*], A.R. Petri [a], A.A. Malafronte [a], J.A.C. Gonçalves [b], S.F. Barros [c,a], C.C. Bueno [b], J.M. Fernández-Varea [d,a], N.L. Maidana [a], M.N. Martins [a], V.R. Vanin [a]

[a] Instituto de Física da Universidade de São Paulo, Rua do Matão 1371, 05508-090, São Paulo, Brazil
[b] Instituto de Pesquisas Energéticas e Nucleares, Comissão Nacional de Energia Nuclear, São Paulo, Brazil
[c] Instituto Federal de São Paulo, Rua Primeiro de Maio 500, Bairro Estação, 08571-050, Itaquaquecetuba, SP, Brazil
[d] Facultat de Física (FQA and ICC), Universitat de Barcelona, Diagonal 645, ES-08028, Barcelona, Catalonia, Spain

A B S T R A C T

Commercial PIN photodiodes, repurposed as particle detectors, have received a lot of attention along the past decades because they can offer a low-cost solution suitable for several applications. The BPX-65 photodiode has been chosen because of its interesting features for measuring electrons in a harsh radiation environment close to the beam of an accelerator. Its electrical characterisation and its application to photon spectrometry have been presented in the companion paper I. Here, its response function (RF) to electrons is investigated using the beam from an electron accelerator with a small energy spread. The empirical expressions for the RF available in the literature have been improved, simplified, and combined to obtain a final form with 7 free parameters: 4 non-linear and 3 linear. A special fitting procedure, which takes advantage of the presence of the linear parameters, is described. The behaviour of these parameters with beam energy and bias is investigated to uncover the physical origin of the three components included in the proposed RF. The interpretation of the features of the spectra is confirmed by Monte Carlo simulations carried out employing the general-purpose PENELOPE/penEasy package. To take into account the charge-collection properties of the device, a simple model has been implemented and is compared to data. It has then been possible to estimate the thickness of the partially dead layer from the experiment.

1. Introduction

The present article, denoted hereafter as paper II, is a companion to paper I (Malafronte et al., 2020), where a low-cost commercial silicon PIN (p-type-intrinsic-n-type) photodiode has been identified, characterised from the electrical point of view, and tested as an x-ray detector. The device is aimed at studying the angular distribution of electrons undergoing single, plural, and multiple elastic scattering in thin metallic foils. In the envisioned setup, the well-collimated beam from an accelerator impinges on a target inside a vacuum chamber. The angular distribution of the electrons is scanned by a detector that can move, inside the chamber, on a circle laying in a plane that contains the beam axis and whose centrer is located at the position where the beam axis crosses the target. The radius of the circle is, for practical reasons, constrained to be around 25 cm; thus the detector has to be equipped with a collimator, whose aperture has a diameter below 0.5 mm, to map with a good resolution the narrow angular distributions ensuing when the foils are thin. The detector is employed to separate electrons that scatter in the foil from electrons with more complicated trajectories, in particular backscattered from other parts of the setup. The possibility to separate elastically and inelastically scattered electrons will also be investigated. Note that for the present purpose such a task needs to be performed on average and not necessarily event-by-event. Two more detectors are fixed on a circle coplanar and concentric with the previous one, but with a larger radius, on either side of the intercept of the beam axis with the target foil to monitor the time stability of its position. Therefore, the detector has to provide a good energy information in the harsh radiation environment close to the beam of an accelerator. As

---

discussed in paper I, the main requirements for a suitable device are: 1) a low-cost solution to allow frequent replacements; 2) a small size to avoid as much as possible an unused area that contributes with unnecessary capacitance; 3) a good energy resolution; and 4) an easy repurposing as a charged-particle detector. The photodiode type BPX 65 manufactured by Osram® fulfils well these constraints. In paper I, a convenient working point at a reverse voltage of 18 V has been found, below the limit of 20 V recommended by the manufacturer for continuous operation. Under such a condition, the measured reverse current, for the four samples studied, is around 0.1 nA (well below the maximum rating of 1 nA declared by the manufacturer) and the total thickness of the depleted and intrinsic regions, estimated from the measured capacitance, is (60 ± 3) µm. The energy resolution (FWHM) found with the γ-rays emitted by ^{241}Am at 59.54 keV is (2.38 ± 0.01) keV. This value is constant, within experimental uncertainties, over an energy range from 10 to 140 keV and close to that obtained with a pulser of (2.39 ± 0.01) keV, indicating that the main contribution is the electronic noise of the setup and the spectrometry chain. Two of the radioactive sources used in paper I (^{133}Ba and ^{57}Co) are enclosed between thin Kapton foils in order to allow for internal conversion electrons to escape. However, because these electrons loose an appreciable fraction of their kinetic energy in the foil, the resulting peaks are displaced and deformed by straggling. Moreover, a significant background by photons and electrons from the various decay lines is always present, hindering a determination of the response function (RF) of the BPX 65 to electrons. A much cleaner way to study the RF is by employing the monoenergetic beam of an accelerator directly impinging on the photodiode, as done in the present paper II. The mentioned thickness of the depleted and intrinsic regions of (60 ± 3) µm corresponds to the range in the continuous-slowing-down approximation (CSDA) of electrons with a kinetic energy of ≈ 85 keV. This indicates that the detector should work well for electrons with energies up to approximately this value, as demonstrated here.

Two approaches have been followed historically to model the RF of a detector: one is to introduce an empirical parameterisation and the other to perform a calculation or a Monte Carlo simulation based on first principles. They both offer complementary advantages. The former allows to reach an accurate description of the data with a smaller effort and is faster for routine use. The values of the parameters can hardly be derived from independent calculations and are obtained by fitting the measurements. Classical works along this line have been made by Tsoulfanidis et al. (1969), Schüpferling (1975), and Damkjaer (1982). The main difficulty is obtaining good agreement with the experimental RF with the smallest number of parameters that, once fitted to the data, must be weakly correlated. When this is achieved, their behaviour is smooth with energy, otherwise the predictive power and the simplicity are lost.

The benefit of Monte Carlo simulations is to produce physical insight on the origin of the contributions that are admitted in the former on an empirical basis. The application of this method to investigate the RF of silicon detectors to electrons begun with the pioneering study by Berger et al. (1969) and continued up to the recent one by Chaoui et al. (2009) through a long history, too extensive to be reviewed here. Usually, the codes are specifically developed in-house. Even when a very good description of the interaction of electrons with silicon is available, it is still necessary to address the issue of how to model the charge-collection properties of the device. In the case of the BPX 65 and of many commercial devices, whose internal structures are not disclosed by their respective manufacturers, it is not a simple task.

The paper is organized as follows. Section 2 describes the experimental setup used to measure the RF with the beam from an electron accelerator. The choice of the working point selected for the BPX 65, which is not supplied by the manufacturer for use as a particle detector, is detailed in paper I and summarised in Section 3. The available empirical models of the RF are presented in Section 4 and their application to the present data in Section 5. In particular, they are simplified and combined in an original form described in Subsection 5.2. The

evolution of the parameters both with the beam energy and with the applied bias is analysed in Subsections 5.4 and 5.6, respectively. As a by-product, it has been possible to investigate the issue of the thickness of the entrance dead layer, as shown in Subsection 5.5. Monte Carlo simulations with PENELOPE/penEasy have also been performed, mostly to back up the identification of the physical origins of the three contributions to the RF, as demonstrated in Section 6. The conclusion of the work is offered in Section 7. Appendix A describes the implementation of the RF and Appendix B the special fitting procedure developed to take advantage of the presence of linear parameters.

2. Experimental setup

The monoenergetic electron beam employed for the present study is produced by the electron gun of the Racetrack Microtron constructed and installed at the Instituto de Física da Universidade de São Paulo, Brazil. Then it passes through a transport system to reach the irradiation chamber. Both are described in more detail by Vanin et al. (2019). The available energies span from 10 to 100 keV with a dispersion of 0.3% at a confidence level of 95% (Vanin et al., 2019). The beam current can be varied between 0.1 nA and 10 µA. The irradiation chamber is kept under vacuum with a residual air pressure of $6.5 \cdot 10^{-5}$ Pa.

As described in paper I, the optical window must be removed from the TO-18 metallic casing of the BPX 65 photodiode before attempting to detect electrons. The device is mounted into an aluminium disc that is then inserted into a holder to allow its positioning perpendicularly to the electron beam inside the irradiation chamber. The signal is delivered with a feedthrough to a pre-amplifier (model 2004 by Canberra® with a noise lower than 2.8 keV at 0 pF) located outside the chamber. The pre-amplifier output is processed by an amplifier (model 572 by Ortec®) with a shaping time of 2 µs and a gain of ≈ 800. Finally, the signals are acquired by a multi-channel analyser (model 927 Aspec by Ortec®).

Early investigations on the repurposing of commercial PIN photodiodes as α-particle detectors, see e.g. the work by Gooda and Gilboy (1987) and the other articles listed in paper I, found the presence of spurious peaks located at lower energies with respect to the main one. This effect was attributed to variations of the charge-collection efficiency or to non uniformities of the optical coating (applied by the manufacturers of photodiodes to reduce the reflection of light) close to the borders of the device. Indeed problems have been found in paper I when the BPX 65 is operated below ≈ 8 V using photons, which constitute a somewhat worst-case scenario because no collimator is employed. They completely disappear above ≈ 8 V. When using electrons, the detector is essentially always sensitive to all the impinging particles and, as a matter of fact, when exposed directly to the accelerator beam, even with the lowest possible currents, the counting rate is too high and causes distortions of the spectra by pulse pile-up in the multi-channel analyser. Therefore, in the present study (with the exception of Fig. 2 below), the BPX 65 is always used with an aluminium collimator, whose diameter and thickness are 0.5 mm and 0.3 mm, respectively. This effectively limits the count rate to a level where pulse pile up is negligible and has the consequence of eliminating any possible distortion due to particles impinging close to the borders of the device. However, the drawback is that the number of impinging electrons cannot be known because the beam current is too low to be measured accurately, ≈ 0.1 nA, and because the beam and collimator parameters are not known with sufficient precision to correct for them. Therefore, the absolute efficiency of the BPX 65 cannot be measured and an absolute confrontation with Monte Carlo simulations, see Section 6, cannot be performed.

To compare the calibrations done with photons and electrons in search of a possible effect of the optical coating and of a partially-depleted entrance layer, see Section 5.5, it is necessary to accurately determine the energy of the beam, E_{beam}. Although E_{beam} is in principle given by the voltage applied to the acceleration electrodes of the gun, a

much better accuracy is achieved by focusing the beam on a very thin target and measuring the emitted x-rays with a silicon drift detector (SDD, model X-123SDD by Amptek®). The energy of the electron beam is determined from the tip of the bremsstrahlung spectrum. In brief, the region around the upper extremum is modelled employing a step function convolved with a Gaussian (Fernández-Varea et al., 2014; Vanin et al., 2016). The free parameters are E_{beam} and the energy dispersion σ_{beam} of the beam. By fitting E_{beam} and σ_{beam} to the data, it is possible to estimate E_{beam} with an accuracy of ≈ 50 eV (Barros et al., 2018). Unfortunately, for impinging electron (and therefore radiated photon) energies above ≈ 60 keV, the efficiency of the SDD becomes too low for such a method to be practically useable. Above 60 keV, the energy of the beam is, therefore, deduced from the voltage applied to the acceleration electrodes of the gun, read with a voltmeter. However, a calibration is needed and it was determined once and for all by a method similar to that described, where the SDD was substituted with a high-purity germanium detector. In this latter case the uncertainty is higher, around ≈ 500 eV.

3. Choice of a working point

The optimal reverse bias of the BPX 65 has been found to be 18 V employing γ- and x-rays in paper I. However, since photons and electrons interact in quite different ways with the device, the response to the latter is also very different and it is not a priori granted that the optimal working point is the same for both. Thus, it is pertinent to check again such a choice with an electron beam. This investigation is reported in Section 5.6 since the results are better discussed in terms of the parameters of the fitted RF introduced in Section 5.2. The main conclusion is that a bias of 18 V is fully adequate both for photons and electrons and is adopted in the present study as the default choice. No spurious peaks are present in all the spectra collected at the working point in paper I or in the present paper II. No instabilities due to runaway avalanche multiplication resulting in discharges have been observed during all the experiments with the electron beam, which represent a different condition from the steady operation as a light sensor anticipated by the manufacturer.

4. The response function to electrons

Photons and electrons deposit their energy in the detector in quite different ways. The former have first to transfer it to one electron of an atom of the medium, either by photoelectric effect or by one or more Compton interactions followed by escape of a lower energy photon, or a final photoelectric effect. Because the first interaction of the photon can happen at any point inside the silicon wafer, the secondary electron tracks are not necessarily originated at the beginning of the depleted and intrinsic regions. In the latter case, the primary electrons start to loose energy as soon as they impact the silicon material and therefore, except for the presence of the optical coating, an ohmic contact, and a partially-depleted layer, always deposit their energy starting from the beginning of the depleted and intrinsic regions. Moreover, electrons suffer elastic collisions with the screened Coulomb field of the atomic nuclei that alter their direction. Since the typical mean free path of the electrons is approximately three orders of magnitude smaller than that of the photons (in the energy interval of interest here, ≈ 10 to 100 keV), the paths inside matter of the former are more irregular than those of the latter, due to considerable multiple elastic scattering. The efficiency of the detector for electrons is almost complete, but a partial loss of signal can happen when the electron is backscattered or its CSDA range is close to the thickness of the depleted and intrinsic regions resulting in a punch through the active region. This brief description should be enough to justify that the RFs for electrons and for photons are fundamentally different and one cannot be used in place of the other. The present paper II is devoted to a study with electrons.

The radiation incident on a semiconductor detector converts, partially or totally, its energy to the production of electron-hole pairs, whose collection induces the electrical signal that is used to determine the energy of the particle (here the focus is only on detectors operated in pulse mode). However, this transfer of energy may be incomplete or some of the generated electron-hole pairs may not be collected. Moreover, the noise of the electronic chain introduces additional fluctuations. Therefore, the measured pulse-height spectrum, $M(E)$, is not the same as the incident energy spectrum of the radiation, $S(E_0)$. The two are related as

$$M(E) = \int_0^{E_{max}} h(E, E_0)\, S(E_0)\, dE_0 \qquad , \qquad (1)$$

where $h(E, E_0)$ is the RF of the detector and E_{max} is the maximum energy of the radiation present in the incident spectrum (i.e. $S(E_0) = 0$ if $E_0 > E_{max}$). If $S(E_0) = \delta(E_0)$ is a Dirac delta function (i.e. the incident spectrum is monoenergetic), the measured distribution $M(E) = h(E, E_0)$ is the RF, which therefore represents the probability density that, when radiation with an energy E_0 impinges on the detector, the registered signal corresponds to an energy in the interval $(E, E + dE)$.

The study of the RF of silicon detectors to photons is a well-developed topic because of its importance for x-ray and γ-ray spectrometry. In general, either radioactive sources with a calibrated activity (see e.g. the work by Barros et al. (2017) and the publications cited therein) or monoenergetic beams from a synchrotron (see e.g. the work by Scholze and Procop (2001) and the publications cited therein) have been employed to such end. The energies involved are typically in the range 50–100 keV in the former case and 5–10 keV in the latter.

The RF of semiconductor detectors to electrons has also received a lot of attention (see e.g. the publications by Planskoy (1968); Berger et al. (1969); Schüpferling (1975); Rehfield and Moore (1978); Otto et al. (1979); Decker et al. (1982); Damkjaer (1982); Clifford et al. (1984); Yamamoto et al. (1988); Frommhold et al. (1991); He et al. (1990); Kojima et al. (1997); Wall et al. (2014); and the other publications cited therein) because it is a fundamental information required, e.g. to unfold β-spectra for producing Fermi–Kurie plots and studying the type of transition or for the determination of end-point energies (Schüpferling, 1975). It is important to note that almost all these works cover energies of the order of 1 MeV and above, where bremsstrahlung emission (and in the case of Frommhold et al. (1991) electron transmission) contributes to the shape of the RF. Here the interest is in energies between 10 and 100 keV, both because they are those to be employed in the measurements of multiple scattering from thin metallic foils, that are our main purpose, and because the BPX 65 cannot be used above this range due to the aforementioned limited thickness of the depleted and intrinsic regions. The only publications of interest for the present study are those by: Planskoy (1968) (electrons with energies between 50 and 625 keV), Schüpferling (1975) (62.52, 363.8, and 624.15 keV electrons), Damkjaer (1982) (electrons with energies of 100–600 keV in steps of 100 keV), Yamamoto et al. (1988) (62.52, 84.23, and 87.32 keV electrons), and Wall et al. (2014) (12.6, 15.6, and 18.6 keV electrons). Planskoy (1968) used both i) conversion electrons from a radioactive source, measuring in coincidence the characteristic x-rays to ensure that they have a well-defined energy, and ii) electrons from a radioactive source filtered with a β-spectrometer. Schüpferling (1975) employed only a source of type i) and Damkjaer (1982) of type ii). Finally, Wall et al. (2014) accelerated electrostatically the electrons extracted by UV rays from a photocathode. Yamamoto et al. (1988) also investigated the RF using conversion electrons from ^{109}Cd with energies of 62.52, 84.23, and 87.32 keV, but without measuring the characteristic x-rays in coincidence and therefore their results are less clean than those of the publications listed above or presented here with monoenergetic electrons.

4.1. The shape of the response function

In general, the investigations by Schüpferling (1975), Damkjaer (1982), Yamamoto et al. (1988), and Wall et al. (2014) agree on the presence of the following three contributions to the RF.

1. A full-energy peak (FEP) corresponding to incident electrons spending all their energy in the production of electron-hole pairs, which are all collected. The two steps are, of course, subject to Poissonian fluctuations and the first one is corrected by the Fano factor.
2. An asymmetric tail to the FEP present only on the lower energy side. This component is not identified by all authors (for instance, Yamamoto et al. (1988) did not introduce it). Its physical origin is not well established in the literature, being usually attributed to (a) energy-loss straggling in the entrance window (Schüpferling, 1975), (b) in the source support foils (Schüpferling, 1975), (c) bremsstrahlung in the detector (Schüpferling, 1975; Damkjaer, 1982) and (d) incomplete charge collection.
3. A low-energy tail (LET) extending from the FEP down to the discriminator threshold. This component has been recognised since the beginning and it is generally attributed to backscattering of the electrons in the detector active volume (see e.g. the work by Planskoy (1968) and the other publications cited therein). To eliminate it, a so-called 4π arrangement, with the source sandwiched between two identical detectors, whose energy signals are summed, has become very popular in β spectrometry (Schüpferling, 1975). The most extensive experimental study of the LET has been published, as mentioned, by Planskoy (1968), who identified three physical processes for its origin: (a) backscattering of the electrons from the active volume of the detector, (b) electrons that lose a fraction of their energy in some other part of the setup, and (c) electrons that are scattered out of the sides of the detector. By using a collimator with a small chamfering angle, Planskoy could reduce sources (b) and (c) and then show that the shape of the LET agrees with the energy distribution of the backscattered electrons measured by other authors, when expressed in terms of the energy deposited in the scattering target. This is a conclusive proof of the presence of mechanism (a).

To analyse the RF, two approaches are possible. One is to employ a detailed first-principles calculation and the second to use a semi-empirical parameterisation. A good example of the former approach is the pioneering work by Berger et al. (1969). The efforts continued in the following years by Schüpferling (1975) and Frommhold et al. (1991) arriving up to the modern ones by Chaoui et al. (2009) (the latter has been developed for the KATRIN (KArlsruhe TRItium Neutrino) collaboration). All these publications described the results obtained with Monte Carlo codes specifically developed in-house. Modern implementations simulate all individual elastic and inelastic collisions to take into account the modifications of the path, the energy loss, and the production of secondary electrons, which are all followed down to a specified energy threshold. The deexcitation of the ionised atoms, which results in the emission of additional secondary electrons, is also included (a better discussion is offered in Section 6). However, beyond an accurate description of the interaction of electrons with silicon, several authors have called the attention on the need to properly model the charge-collection efficiency of the device (Goto, 1993, 1998; Hartmann et al., 1996; Renschler, 2011; Wall et al., 2014). This task is particularly difficult in the case of a proprietary one, like the BPX 65, for which the internal structure, e.g. the doping profiles, are not disclosed in the datasheet by the manufacturer. From these comments it should be clear that the complete simulation of the RF from first physical principles is a very demanding task, which also remains at least partially to be completed. Here we adopt instead an empirical parameterisation to fit the RF and study its features. To confirm that the physical origin of each

term introduced in the RF has been correctly identified, but not to reproduce in detail its shape, a Monte Carlo simulation with the general-purpose code PENELOPE/penEasy (Baró et al., 1995; Sempau et al., 1997, 2011; Salvat, 2019) is also presented in Section 6.

4.2. Analytical expressions of the response function

The simplest model of the RF to electrons was introduced by Tsoulfanidis et al. (1969) for plastic scintillators and applied to silicon detectors by Yamamoto et al. (1988). It is given by an intrinsic part, consisting of a Dirac delta function, representing the FEP (see the contribution 1 above), plus a constant background below it, representing the LET (see the contribution 3 above),

$$f_{\mathrm{T}}(E, E_0) = (1 - \beta)\, \delta(E - E_0) + \frac{\beta}{E_0}\, \Theta(E_0 - E) \tag{2}$$

to be convolved with a Gaussian function to account for the effect of fluctuations (see e.g. Eq. (A.1)). The result is a closed analytical expression (Tsoulfanidis et al., 1969). The adjustable parameter β represents the fraction of the LET relative to the total (i.e. $0 \le \beta \le 1$), Θ is the Heaviside step function, and δ is the Dirac delta function. Tsoulfanidis et al. (1969) correctly attributed the physical origin of the LET to electron multiple scattering in the detector.

An improvement to this model was introduced by Schüpferling (1975), who noted a tail on the lower side of the FEP (see contribution 2 above) that he could not reproduce with his Monte Carlo code (which did not include a description of incomplete charge collection) and attributed it to unaccounted mechanisms that cause losses of the energy of the primary electrons or disappearance of the generated electron-hole pairs. Therefore, he proposed to add to Eq. (2) a third term with an exponential

$$f_{\mathrm{S}}(E, E_0) = (1 - \beta - w)\, \delta(E - E_0) + \frac{\beta}{E_0}\, \Theta(E_0 - E)$$
$$+ w\, \frac{1}{d\,(1 - e^{-E_0/d})}\, e^{-\frac{E_0 - E}{d}}\, \Theta(E_0 - E)\,, \tag{3}$$

where w is now the weight relative to the total of this new contribution (i.e. $\beta \ge 0$, $w \ge 0$, and $\beta + w \le 1$) and d controls the damping of the exponential part. Again, the convolution with a Gaussian yields a closed analytical expression (Schüpferling, 1975).

Damkjaer (1982) proposed a completely different expression for the LET (see the contribution 3 above) of the form

$$h_{\mathrm{D}}(E, E_0) = A\, \frac{\sin(p\,(1 - E/E_0)\,\pi)}{1 + C \exp\left(-\frac{(E/E_0)^2}{\alpha}\right)}\,, \tag{4}$$

where A, p, C, and α are free parameters eventually depending on E_0. While Eq. (4) does not have to be convolved with a Gaussian, on the contrary of Eq. (3), it still misses terms corresponding to the contributions 1 and 2 above. However, Eq. (4) describes much better the contribution 3 to the RF, which is generally not flat, as assumed by Eq. (3), but has instead a broad maximum in the lower half of the energy range. As a matter of fact, Eq. (4), when modified as discussed in Section 5.2, provides a quite good fit to the experimental data obtained in the present work as well. For the sake of completeness, it should be mentioned that the full expression of Eq. (4) given by Damkjaer (1982) contains another term to include the effect of bremsstrahlung (entering into the contribution 2 above), which is not important at the energies considered here.

Since the mathematical form of Eq. (3) or (4) lacks a direct physical interpretation, the parameters cannot be calculated from first principles, but can only be determined by fitting the measured RFs. However, as noted by Clifford et al. (1984), for the model to be acceptable and to have a minimum predictive power, the parameters must depend on E_0 in

a well-behaved continuous form. In such a case, a parameterisation of their values as a function of E_0 can be found and the RF obtained for any energy E_0 in the measured range. If this is not possible, the model turns, of course, largely useless. This general idea introduced by Clifford et al. (1984), while studying the electron RF using the beam with a well-defined energy from a beta spectrometer, was applied more recently by Zevallos-Chávez et al. (2001) to investigate the photon RF employing radioactive sources. It is followed here as well, profiting from the monoenergetic electron beam of an accelerator.

4.3. Resolution

The issue of the origin of fluctuations in the response is a classical topic (Knoll, 2010) that was thoroughly studied with photons for both Si (Li) (Hollstein, 1970) and HPGe (Owens, 1985) detectors. The resolution is usually quantified adopting the standard deviation of a Gaussian whose parameters are fitted to the FEP. Its expected behaviour is (Hollstein, 1970; Owens, 1985; Scholze and Procop, 2001)

$$\sigma^2 = \sigma_{el}^2 + \sigma_{cc}^2 + w_{eh} \, F \, E_{dep} \qquad , \qquad (5)$$

where the first term is the contribution of electronic noise to the variance, σ_{el}^2, the second term represents the fluctuations in the collection of the electron-hole pairs, σ_{cc}^2, and the third one those in their generation. The symbols E_{dep}, w_{eh}, and F, appearing in Eq. (5), represent the energy deposited in the active volume of the detector, the average energy spent to produce an electron-hole pair, and the Fano factor, respectively. While σ_{el}^2 only depends on the spectroscopy chain and the electronic characteristics of the detector (i.e. its capacity and reverse current (Hollstein, 1970; Owens, 1985)), σ_{cc}^2 is affected by the electric field in the device and the location of the produced electron-hole pairs (thus it is sensitive to the bias, the energy of the photons, and the illumination conditions (Hollstein, 1970; Owens, 1985)). No detailed study with electrons has been published, to the best of our knowledge. It is tempting to identify the quantity σ appearing in Eq. (5) with the standard deviation of the Gaussian representing the fluctuations mentioned in the previous Section 4.2, see also Eq. (A.1). This is certainly correct, considering the FEP, for the first and last terms, but some care is possibly necessary to avoid double counting of the fluctuations in the charge collection efficiency when they are described by a specific term of the RF like in Eq. (3). The use of Eq. (5) is questionable and certainly more difficult for the LET, when the required convolution is with a Gaussian whose standard deviation depends on the deposited energy. Fortunately, these issues are of no concern in the present work, where Eq. (5) is dominated by the energy-independent term σ_{el}^2, see Section 5.4, and no convolution is needed for Eq. (4).

5. Experimental investigation of the response function to monoenergetic electrons

The RF of the BPX 65 photodiode to monoenergetic electrons has been investigated with the setup described in Section 2 from 10 to 100 keV. The energy of the beam has been determined as also outlined in Section 2.

5.1. Experimental procedure

The pile-up of events within the resolving time of the multi-channel analyser can result in the appearance of counts above the FEP that would need quite some additional efforts to be deconvolved or modelled, like done e.g. by Clifford et al. (1984). To avoid the distortion of the shape of the RF, the beam current is adjusted to keep, in all cases, the count rates below ≈ 300 Hz. The acquisition of a full spectrum takes between ≈ 5 to ≈ 20 minutes and a full run around a few hours. Therefore, it is not necessary to monitor the stability of the electronic chain with a pulser as

done in paper I where photons from radioactive sources were used.

The first step in the analysis of the RF is to subtract the background, which has been determined in a separate measurement without beam. To maintain the same conditions in terms of electronic noise, the accelerator is kept switched on, but the electron beam is deflected outside the irradiation chamber. The background spectrum is acquired during the same time as a typical measurement with beam in the chamber, and the result normalised to the acquisition live time of the latter. The same background spectrum is employed for all beam energies. Such a procedure is demonstrated in Fig. 1 for the spectrum corresponding to 10.39 keV electrons. The noise increases strongly close to the discriminator threshold. Consequently, its subtraction is important when this shoulder is not well separated from the FEP, i.e. for energies below 30 keV with the present setup.

5.2. Adopted form of the response function

Spectra of a 97 keV electron beam are shown in Fig. 2. An almost constant LET is clearly present in the results obtained here as has also been found in all previous works on the RF, (see contribution 3 in Section 4.1). It has a broad maximum in the lower half of the energy range between the lower threshold and the FEP. The asymmetry on the lower side of the FEP noted by Schüpferling (see contribution 2 in Section 4.1) and introduced in his model, see Eq. (3), is also clearly visible. However, a direct use of Eq. (3) is not adequate in the present case, owing to the mentioned maximum in the LET, which is, on the contrary, taken into account in Eq. (4). So it is necessary to combine Eq. (3), which is adequate to describe contributions 1 and 2, with Eq. (4), which is the best to reproduce contribution 3. Nevertheless, before starting to do this, it is interesting to check if the observed behaviour of the RF comes from the detector itself or from the setup.

Two tests have been made to exclude the possibility that it is originated by the collimator. In the beginning, a collimator with a thickness
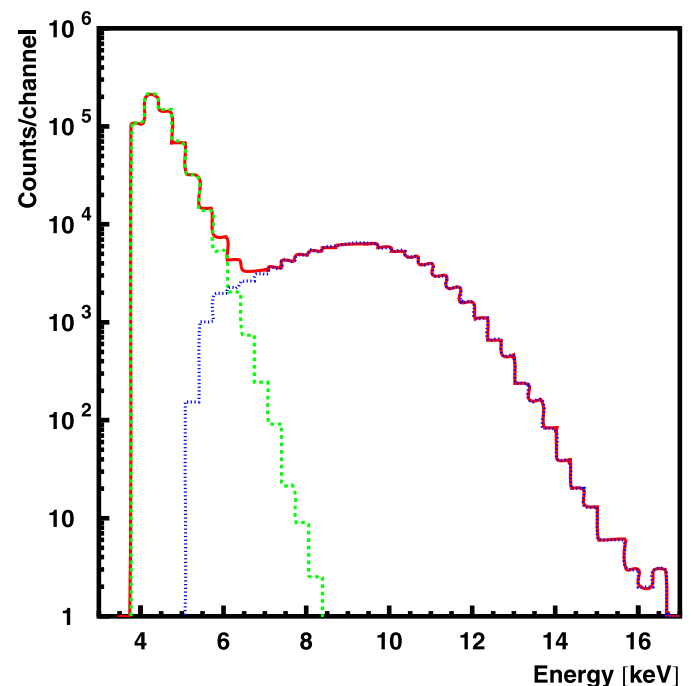

Fig. 1. Example of the subtraction of the background from a spectrum measured with a repurposed BPX 65. The spectrum obtained with a beam of electrons with a kinetic energy of 10.39 keV and when the beam is deflected outside the irradiation chamber are represented with a continuous and a dashed histogram, respectively. The latter is normalised to the same live time as the former. The dotted histogram is the result of the subtraction of the background. The energy dispersion is 0.33 keV/channel.
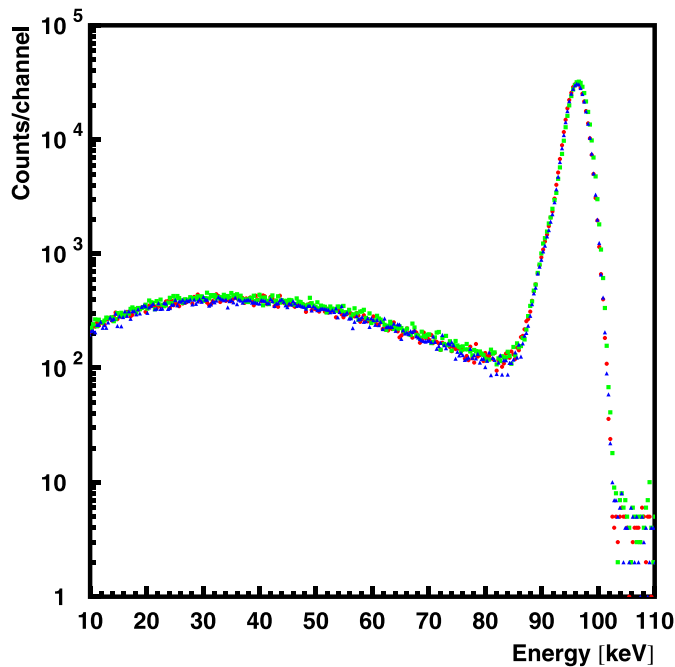
Fig. 2. Spectra of a 97 keV electron beam collected employing a collimator with a thickness of 1.0 mm (●), of 0.3 mm (■), and of 0.3 mm covered with a carbon mask (▲). The energy dispersion is 0.33 keV/channel.

of 1.0 mm has been employed. Since this is not strictly necessary to stop electrons with energies up to 100 keV, the highest available in the present setup (see Section 2), the thickness of the very same collimator has been reduced once and for all to 0.3 mm (which has been employed in all the following measurements). Two spectra have been acquired, one before and one after such a change, for the same duration of 5 min: they are compared in Fig. 2 after normalisation for the same live time (300 s). No difference is observed, thus excluding any relevant influence of electrons incident at grazing angles on the border of the collimator or producing bremsstrahlung photons, while stopping in the bulk of the collimator material, that are detected. As a matter of fact, Planskoy (1968) also made a study of the influence of the chamfering angle of the collimator on the RF, suggesting that the closer to a straight hole the better to avoid distortions. In the present case, no chamfering has been made. To further exclude any effect of bremsstrahlung photons generated in the bulk of the collimator, a third test has been performed covering the 0.3-mm-thick collimator with a carbon mask (which has approximately half the atomic number and therefore generates one quarter of the bremsstrahlung) with a hole with a diameter of 1.0 mm. Again the spectrum acquired during a time interval of 5 min is plotted in Fig. 2 after normalisation to the same live time. No difference is observed. This gives confidence in the fact that the broad maximum in the LET is really a feature of the BPX 65 and not of the present setup and therefore it has to be introduced in the model of the RF. Since the carbon mask does not reduce the LET, all the other spectra shown here have been measured without it.

The typical RF illustrated in Fig. 2 has all the features 1, 2, and 3 described in Section 4.1. To fit it, a new model has been introduced that is not listed in Section 4.2. For contributions 1 and 2, namely the FEP and the asymmetry on the lower side of the FEP, respectively, the corresponding terms in Eq. (3) are retained resulting in a Dirac delta function and an exponential convolved with a Gaussian. Actually, a small inconsistency present in the form of the convolution of Eq. (3) adopted by Schüpferling (1975), Clifford et al. (1984), Yamamoto et al. (1988), and He et al. (1990) has been corrected. The full expressions are given in Appendix A. The physical origin of component 2 is not clear. As mentioned in Section 4.1, the possible sources are: (a) energy-loss

straggling in the entrance window, (b) in the source support foils, (c) bremsstrahlung in the detector, and (d) incomplete charge collection. In the experimental conditions of the present work, (b) can be excluded because the beam is monoenergetic with an energy dispersion of 0.3% (see Section 2) and (c) because the energies of interest of at most ≈ 100 keV are too low to result in a significant bremsstrahlung emission (the radiation yield of 100-keV electrons in silicon is 0.014% (Berger et al., 1984, 2017), and it is even smaller for lower energies). Investigations with a Monte Carlo code by Schüpferling (1975) independently confirm that (c) cannot explain the origin of contribution 2 even at energies of 364 keV. The roles of (a) and (d) can only be assessed by a comparison with simulations, as done in Section 6. For contribution 3, Eq. (4) has been tested first. As recommended by Damkjaer (1982), the parameter α is kept fixed to the value 0.0351. Rather small values of p, below 0.1, have then been obtained from the fit to the measured RFs. This means that the argument of the sine is at most of order $p\,\pi \lesssim 0.3$, for which the deviation of $\sin x$ from x is ≈ 1.5%. To avoid the strong instabilities resulting from the correlations between parameters p and A, it has been decided to linearise the sine and replace Eq. (4) with

$$h_3(E, E_0) = A \frac{1 - E/E_0}{1 + C \exp\left(-\frac{(E/E_0)^2}{\alpha}\right)} \qquad , \qquad (6)$$

effectively eliminating the parameter p. More details about the actual expressions employed for the complete RF are given in Appendix A. Having so simplified Eq. (4), a test has been carried out to compare two ways to fit the complete expression of the RF with Eq. (6) representing contribution 3. In the first case, α is fixed to 0.0351 while, in the second, it is left free to be adjusted. This leads only to a marginal improvement of the $\chi^2/\text{n.d.f.}$, e.g. from 1.13 to 1.08 for the spectrum measured at 100.03 keV. Given the extra complexity of having to deal with one more dimension in the fit and having to study the evolution of α with electron energy and bias voltage, it has been decided to follow the recommendation by Damkjaer (1982) and keep $\alpha = 0.0351$ in the present work. As mentioned in Section 4.1, the possible sources of contribution 3 are: (a) backscattering of the electrons from the active volume of the detector, (b) electrons that loose a fraction of their energy in some other part of the setup, and (c) electrons that are scattered out of the sides of the detector. Since the detector is used with a collimator, (c) can be excluded and the tests described above rule out an important role of (b) for the internal wall of the collimator hole. Again, the dominant role of (a) can only be assessed by a comparison with simulations as done in Section 6.

5.3. Fit of the response function to the data

The parameterisation of the RF introduced in the previous Subsection 5.2 has 7 adjustable parameters in total: 4 non-linear, i.e. E_0, σ, d, and C (see Eqs. (3) and (6) or Appendix A), and 3 linear, i.e. N_1, N_2, and N_3 (the normalisations of the three contributions, see Appendix A). A fitting procedure has been especially developed to take advantage of the presence of the linear parameters by treating them separately and efficiently. The iterative minimisation is only applied to the non-linear parameters. This method is described in Appendix B.

The fitting of the non-linear parameters is the most difficult part and the convergence of the minimisation procedure can be largely improved by selecting good starting values. Once these initial estimates have been found, they need not be modified for the entire energy range from ≈ 10 to ≈ 100 keV covered here, with the obvious exception of the starting value of the position of the FEP. In the worst case, approximately one thousand iterations, with approximately one thousand points in the spectrum, are necessary for full convergence, which is achieved in tens of seconds on a modern computer with a 64-bit CPU running at 2.0 GHz (opteron 6128 HE manufactured by AMD®). To ensure convergence of the minimisation procedure, it has been found necessary to introduce a window on the allowed range of the parameters. The selected interval is,

however, quite large and in no case any of the estimated parameters is close to the limits (with the exception of parameter C under the conditions discussed below). The quality of the minimum of χ^2, $\chi^2_{\min}$, can be inspected by plotting the contours corresponding to $\chi^2 = \chi^2_{\min} + n^2$ for any pair of fit parameters (the χ^2 being minimised with respect to the other fit parameters) and verifying that they have closed elliptical shapes without strong deformations. The case corresponding to electrons with an energy of 100.03 keV for $n = 1$ and 2 is displayed in the supplemental material to confirm that χ^2 shows a good minimum. The largest correlation coefficient, in absolute value, is found between d and E_0 and amounts to -0.67.

Four examples of the fit to the measured RFs are shown in panels (a), (b), (c), and (d) of Fig. 3 for electrons with an energy of 100.03, 60.03, 30.90 and 10.39 keV, respectively. Each of the contributions 1, 2, and 3, is also displayed separately. The agreement is quite good for all energies (those shown in Fig. 3 and the others measured for the present work) proving the flexibility and accuracy of the selected expression.

One last issue, however, deserves to be addressed. To avoid a large dead time, it is necessary to acquire the experimental spectra with a lower threshold equivalent to ≈ 3 keV. A small part of the measured RF, below ≈ 7 keV, is distorted by the non-ideal behaviour of the electronic chain resulting in an incorrect modelling of the subtracted background, see Subsection 5.1, immediately above the threshold and has been omitted from the fit and from Fig. 3 (all the range shown has actually been employed). Independently from the exact value of the threshold, it is rather obvious that, for low beam energies, only contribution 1 is well contained in the fitted interval, contribution 2 is partially included, while contribution 3 is only marginally present (see panel (d) in Fig. 3). Therefore, it is impossible to expect that the parameter C, needed to describe the LET, see Eq. (6), can be fixed with any accuracy in such a case. Under the present conditions, this happens below approximately

40 keV. Therefore, and only for 30.90 keV and below, C is determined by linearly extrapolating its behaviour from higher energies, see also Section 5.4. No problem has been found for the convergence of the other parameters, whose best estimates remain far from the limits of their allowed range.

5.4. Evolution of the parameters with electron energy

As mentioned at the end of Section 4.2, a good parameterisation of the RF must, beyond reproducing well the data, possess a smooth evolution of the parameters as a function of electron energy. Otherwise its predictive power (i.e. its ability to describe the situation for an energy that is not among those that have been directly measured) is absent and its usability is very limited. This issue has been investigated by collecting data at 13 energies from 10.39 to 100.03 keV. The spectra obtained in 4 cases are shown in Fig. 3, but they represent well all the others. The evolution of all the 7 parameters of the RF is displayed in Fig. 4: the 4 non-linear ones, i.e. σ (converted to FWHM), d, C, and E_0 in panels (a), (b), (c), and (d), respectively, and the 3 linear ones, i.e. N_1, N_2, and N_3, in panel (e). Finally, the reduced χ^2 of the fits is reproduced in panel (f). The uncertainty bars are statistical only and correspond to one standard deviation (see Appendix B for more details on the fitting procedure and on how the uncertainties are estimated) except that for panel (d), see Section 5.5.

The σ of the Gaussian is included in the convolution of contributions 1 and 2 (see Section 4) to represent the fluctuation in the generation of the electron-hole pairs, in their collection, and the noise of the electronic chain. In the present data, it is essentially constant, considering the uncertainty bars shown in Fig. 4 (a). The value obtained by the average, weighted with the statistical uncertainties of the points, is represented by the green dashed horizontal line in Fig. 4 (a). It is equal to
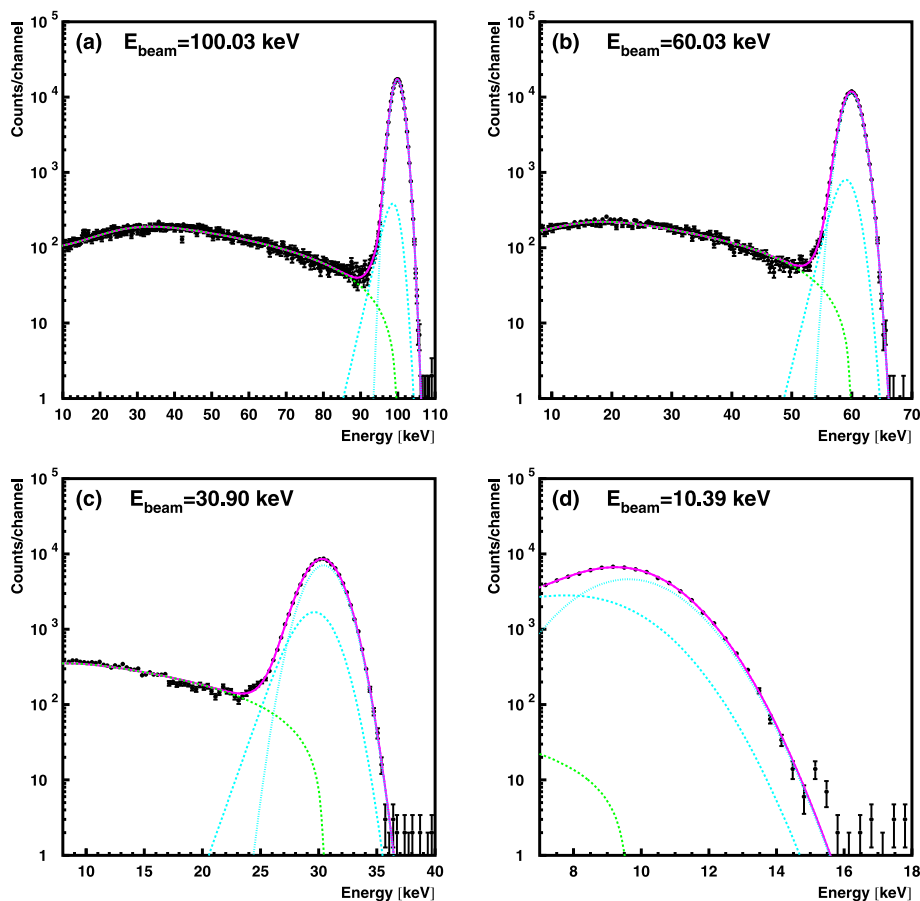

Fig. 3. The curves represent the RF proposed here (see Subsection 5.2 or Appendix A) with parameters fitted to the experimental data, shown as points with uncertainty bars. The spectra have been measured employing monoenergetic electrons with energies of 100.03 (a), 60.03 (b), 30.90 (c), and 10.39 keV (d). The contributions 1 (FEP - cyan dotted curve), 2 (asymmetric tail on the lower side of the FEP - cyan dashed curve), 3 (LET - green dashed curve), and the total (magenta continuous curve) are plotted separately. The uncertainty bars, representing the statistical contribution alone, correspond to one standard deviation. The energy dispersion is 0.33 keV/channel. (For interpretation of the references to colour in this figure legend, the reader is referred to the Web version of this article.)
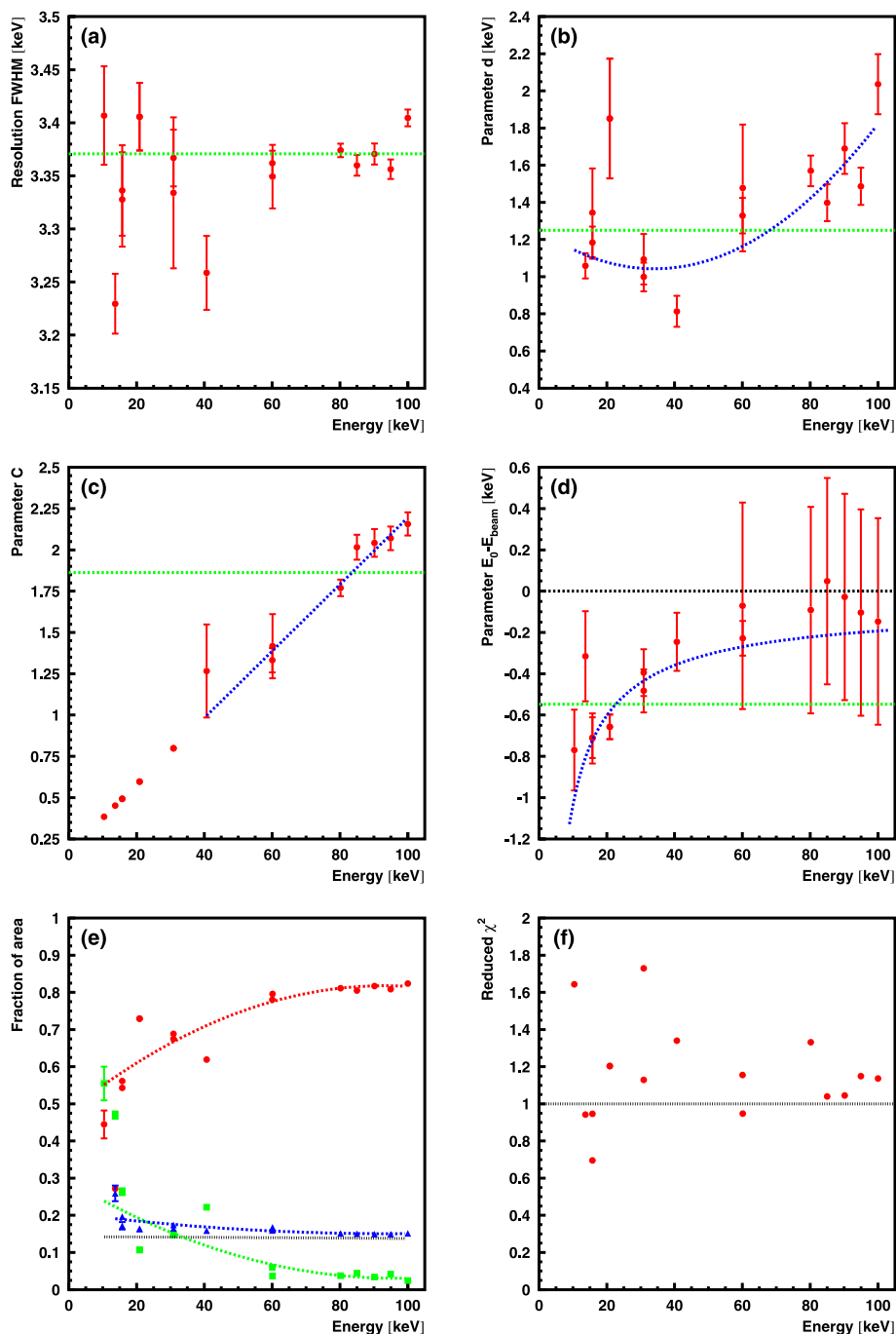
Fig. 4. Behaviour of the parameters of the model of the RF proposed here (see Subsection 5.2 or Appendix A) with the energy of the monoenergetic beam of electrons. There are 7 free parameters in total. The 4 non-linear ones, i.e. σ, d, C, and E_0 (see Eqs. (3) and (6) or Appendix A), are shown in panels (a), (b), (c), and (d), respectively. The 3 linear ones, i. e. N_1, N_2, and N_3, which are the normalisations of the contributions 1 (FEP), 2 (asymmetric tail on the lower side of the FEP), and 3 (LET), are displayed in panel (e) with red bullets, green filled squares, and blue filled triangles, respectively. Finally, the reduced χ^2 of the fit is plotted in panel (f). The green dashed horizontal lines in panels (a), (b), (c), and (d) indicate the average, weighted with the statistical uncertainties of the points. The blue dashed curves in panel (b), (c), and (d) are a fit of the parameters of a parabola, of a straight line, and of the thickness of the dead layer, respectively. The dashed curves in panel (e) are fits of the parameters of a parabola to the series of points with the corresponding colours. Finally, the black dotted curve in panel (e) is the fraction of backscattered electrons according to the parameterisation proposed by Tabata et al. (1971). (For interpretation of the references to colour in this figure legend, the reader is referred to the Web version of this article.)

(3.371 ± 0.003) keV, higher than the value of (2.38 ± 0.01) keV reported in paper I. However, it matches well the resolution obtained with a pulser in the current setup: (3.30 ± 0.04) keV. Thus, the main origin of the values of σ encountered in the data is the noise from the electronic chain, as also found in paper I, and little margin is left for other contributions. The term linear with E_{dep} in Eq. (5) can be evaluated assuming that all the energy of the impinging electron is deposited in the active volume, in the case of the FEP, and choosing reasonable estimates of the parameters ($w_{eh} = 3.66$ eV and $F = 0.114$ (Scholze and Procop, 2001) or $w_{eh} = 3.58$ eV and $F = 0.135$ (Gao et al., 2007)). The numerical results are 150–160 and 480–520 eV FWHM for $E_{dep} = 10$ and 100 keV, respectively, confirming the above conclusion. The differences with paper I are related to the changes in the preamplifier, i.e. model A250 by Amptek® versus model 2004 by Canberra®, and in the setup. In paper I,

the BPX 65 is installed inside a smaller chamber, it is directly connected to the preamplifier, and only a radioactive source is present to produce the γ- and x-rays (therefore the accelerator is not needed and it is kept switched off during the acquisition of the spectra). Here the preamplifier has been mounted on the outside of the irradiation chamber of the accelerator beamline (see Section 2), it has been connected to the detector by a 50-cm-long cable and, of course, the accelerator is turned on. Thus, the electronic noise environments are rather different in paper I and here, the former being, obviously, less affected by disturbances.

The case of the parameter d, i.e. the energy scale of the exponential present in contribution 2, see Eq. (3), is different. Again, the average, weighted with the statistical uncertainties of the points, is represented by the green dashed horizontal line in Fig. 4 (b). A deviation from a constant behaviour is seen above ≈ 80 keV. A fit of the parameters of a

parabola is also shown in Fig. 4 (b) with a dashed blue curve: it clearly reproduces the situation better and seems to indicate an increase of d both at the high- and low-energy ends of the range covered. In general, a larger value of d indicates an exponential tail that decreases more slowly and corresponds to a stronger deformation of the lower side of the FEP. As discussed in Section 5.2, it is highly unlikely that bremsstrahlung contributes significantly to the RF at and below ≈ 100 keV. If the origin of contribution 2 is attributed to incomplete charge collection, such a behaviour can result both because the energy deposition happens inside the low-field region at the front of the device or partially outside the depleted and intrinsic regions closer to the back, in both cases increasing the importance of diffusion and recombination. The thickness of the latter has been found in paper I to be (60 ± 3) μm for the selected working point of 18 V (see Section 3), corresponding to the CSDA range of electrons of ≈ 85 keV. Therefore, the increase of d above ≈ 80 keV can be interpreted as resulting from a partial deposition of the energy outside the active part of the detector. On the other hand, the increase below ≈ 30 keV corresponds to an energy deposition happening predominantly inside the low-field region closer to the ohmic contact on the front. Nevertheless, it should be noted that below a few tens of keV and with the electronic chain employed here, the lower part of the FEP is already hidden below the discriminator threshold, see e.g. Fig. 3 (d), and the determination of the parameter d from the fit is more uncertain.

The behaviour of the parameter C, appearing in Eq. (6), adopted here to describe contribution 3, is displayed in Fig. 4 (c). The green dashed horizontal line has the same meaning as in Fig. 4 (a) and (b), clearly indicating that a simple constant does not reproduce the data. However, a linear fit, shown with a blue dashed line in Fig. 4 (c), matches well the points down to 40.65 keV. It is not surprising that C decreases with energy, since it controls the position of the broad maximum in the LET, that is decreasing with energy even in relative terms to the position of the peak, as it is visible from Fig. 3 (e.g. compare panel (a) and (b)). At $\approx$ 30 keV and below, this maximum has already disappeared from the part of the spectrum measured above the discriminator threshold, as mentioned in Section 5.3, see also Fig. 3 (c) and (d). Correspondingly, the fit cannot determine the value of C with any reliability. Thus, at 30.90 keV and below, C is not considered a fit parameter anymore: instead its value has been fixed by extrapolating the linear behaviour from the fit in the energy range from 100.03 to 40.65 keV (i.e. the mentioned blue dashed straight line in Fig. 4 (c)).

Once the RF has been fitted, the position of the FEP, i.e. the parameter E_0 in Eqs. (3) and (6), can be extracted. Since it agrees rather well with the beam energy, only the difference is plotted in Fig. 4 (d). If no other effect is present, the points should fluctuate, within their uncertainty bars, around zero, i.e. the black dashed horizontal line. This does not happen. The green dashed horizontal line represents again the weighted average, and it also does not fit the data either. The actual behaviour is more complex due to the energy loss in the entrance dead layer, displayed by the dashed blue line in Fig. 4 (d). By adjusting the curve to the measurements, it is possible to estimate the thickness of the inactive part of the detector, as discussed in more detail in Section 5.5. This is the only case where the uncertainty bars shown in Fig. 4 include another contribution beyond that of the fit of the RF, see again Section 5.5.

The fractions of the area of the RF associated to each of the contributions, i.e. $N_1/(N_1 + N_2 + N_3)$, $N_2/(N_1 + N_2 + N_3)$, and $N_3/(N_1 + N_2 + N_3)$, are shown in Fig. 4 (e) with red bullets, green filled squares, and blue filled triangles, respectively. The dashed curves are fits of the parameters of a parabola to the data represented with the same colour. Except for the measurements at 20.86 and 40.65 keV, the behaviour of the points is generally regular, while the uncertainty bars are underestimated. An exception is represented by the rapid increase of $N_2/(N_1 + N_2 + N_3)$ below ≈ 15 keV. However, it is important to remember again that, under these conditions, a part of the asymmetry on the lower side of the FEP is already hidden below the discriminator threshold, see e.g. Fig. 3 (d), and the determination of its area becomes quite uncertain.

A more careful study with an improved electronic chain is necessary to decide if such a feature is present and how it should be modelled. With increasing energy, the RF is more and more dominated by the FEP while the importance of the exponential tail on its lower side decreases. This is consistent with the fact that the electrons penetrate more into the detector and therefore deposit their energy in deeper layers. Those are further apart from the ohmic contact and closer to or in the high-field region where charge collection is more efficient. The fraction of the area associated to the LET, $N_3/(N_1 + N_2 + N_3)$, is almost constant above 30 keV. It corresponds well with the empirical parameterisation of the fraction of electrons backscattered from silicon proposed by Tabata et al. (1971). These authors state that their formula cannot be applied below 50 keV, thus the discrepancy with measurements at low energies is not necessarily an indication of the presence of another mechanism. On the contrary, such an agreement is the first evidence presented here that contribution 3 is really associated to the electrons that are backscattered from the silicon crystal and therefore deposit only part of their energy in the active volume, as found also experimentally by Planskoy (1968), see Section 4.1. Other arguments to support the same conclusion come from the independence of C from the bias, see Section 5.6, and the comparison of the shape of the LET with the Monte Carlo simulations presented in Section 6.

Finally, the reduced χ^2/n.d.f. of the fits to the measured RFs are presented in Fig. 4 (f). To give an idea, the number of degrees of freedom is 24, 81, 169, and 286 at 10.39, 30.90, 60.03, and 100.03 keV, respectively. The black dashed horizontal line represents the ideal value of 1. In general, the proposed model fits rather well the measurements for all energies with two exceptions: one with χ^2/n.d.f. = 1.5 and n.d.f. = 24 and one with χ^2/n.d.f. = 1.7 and n.d.f. = 81, corresponding to a probability to observe a larger value of χ^2 of $2.5 \cdot 10^{-2}$ and $5.1 \cdot 10^{-5}$, respectively. No particular trend can be identified, indicating that the proposed parameterisation is applicable over all the beam energy range investigated.

5.5. Determination of the dead layer thickness

Although the BPX 65 has been used here after removing the optical window (see Section 2), there is an inherently inactive layer in all diodes, called dead layer, due to the presence of an ohmic contact and a possible partially-depleted highly-doped region. Moreover, devices intended to be used to detect optical photons, also have a coating to reduce the reflection of light. Therefore, the impinging electrons can lose energy in these structures without generating any signal or with only a partial collection due to diffusion of the minority charge carriers to the depleted region (Wall et al., 2014; Zhao et al., 2016).

A classical method to determine the thickness of the dead layer is to measure the shift in energy for charged particles entering at various angles in the detector (Knoll, 2010). It is normally performed with α particles, see e.g. the work by Yamamoto et al. (1988), because of their high energy loss per unit path length and their almost straight trajectories. It has also been tested with electrons by Wall et al. (2006) selecting a beam energy of 20 keV, well within the range considered here. However, the main difficulty is that a provision is needed in the setup to tilt the detector and measure its inclination angle accurately. There is not such a device installed in our chamber, therefore we have to proceed in a different way.

Another method, also employed by Wall et al. (2006), can be used if the energy of the beam, E_{beam}, can be determined very accurately: the presence of the dead layer can be inferred from the mismatch between this energy and that corresponding to the FEP seen by the detector at E_0. Wall et al. have compared the two approaches and found a difference of $\approx 8\%$, a factor of ≈ 2 larger than their estimated uncertainties. It is important to note that both methods depend on the knowledge of the energy loss, introducing an unavoidable uncertainty. In the present setup, it is possible to determine E_{beam} with high precision from the

bremsstrahlung spectrum measured with a thin target, see Section 2. The largest sensitivity to the thickness of the dead layer is achieved for $E_{beam} \lesssim 50$ keV, where the uncertainty is ≈ 50 eV (Barros et al., 2018) (see Section 2). Wall et al. (2006) assumed a linear relation between E_0 and E_{beam}, effectively excluding an offset in their calibration, to be able to determine the proportionality constant between energy and channel and the thickness of the dead layer with one fit. Here, this extra assumption is avoided and we make use of an accurate linear energy calibration, constructed in two parts. Below 60 keV, photons emitted by radioactive sources are employed, following paper I, since the positions of the ensuing FEPs are not affected by the presence of a dead layer. The efficiency of the detector for photons of higher energies is quite low, see again paper I, requiring days to acquire a spectrum with good statistics and a close monitoring of the stability of the electronics. Therefore, above 60 keV, the calibration relies on the same measured spectra used in Section 5.4 to study the RF, since at these energies the effect of the dead layer is small for electrons as well. The plot of $E_0 - E_{beam}$ as a function of E_{beam} has actually already been shown in Fig. 4 (d). As commented in Section 5.4, there is clear evidence that $E_0 - E_{beam}$ does not fluctuate around zero within the uncertainty of the data and that a simple constant shift also does not explain the observed behaviour: the average $E_0 - E_{beam}$ goes to zero for higher values of E_{beam}, as expected from the presence of a thin dead layer. The experimental values of $E_0 - E_{beam}$ have been fitted by a calculation of the energy lost in the dead layer, assumed to be made of Si, using the ICRU Report 37 (Berger et al., 1984) through the ESTAR database of electron stopping powers (Berger et al., 2017). Note that the correct evaluation of the energy lost during slowing down is performed instead of taking just the value corresponding to E_{beam} for the full thickness of the dead layer (e.g. this amounts to an increase by 4% of the energy lost by 10 keV electrons in the thickness given below). Since the only free parameter is the thickness of the dead layer, it can be determined, together with its statistical error, by the least-squares method by finding χ^2_{min}, i.e. the minimum of χ^2. The uncertainty bars shown in Fig. 4 (d) are indeed used to evaluate the χ^2. They are obtained as the quadratic sum of the uncertainty in E_0, returned by the fit of the RF, with the uncertainty in E_{beam}. The latter is really of statistical origin only below 50 keV, coming from the fit of the tip of the bremsstrahlung spectrum (see Section 2). Above 50 keV, it rather represents a systematic uncertainty and it blows up the size of the uncertainty bars shown in Fig. 4 (d). Although this is somewhat inconsistent, the sensitivity to the thickness of the dead layer is small above 50 keV and the larger uncertainties still decrease the weight of those data. The minimum of χ^2 gives $(253 \pm 13 \pm 8)$ nm, where the first uncertainty is given by a variation from χ^2_{min} to $\chi^2_{min} + 1$ and the second one is purely systematic, obtained by propagating the declared uncertainty of the stopping power tables of 3% (Berger et al., 1984). The blue dashed curve in Fig. 4 (d) corresponds to the calculated $E_0 - E_{beam}$ for the best estimate of the thickness of 253 nm. The only other result for the BPX 65 that we have found was published by Jakšić et al. (2005) as being 300 nm but without a description of the adopted method or a determination of the corresponding uncertainty. Therefore, we conclude that our results are in good overall agreement.

There are, however, other sources of uncertainties on the thickness of the dead layer.

i The exact composition of the dead layer is not disclosed by the manufacturer. There is an ohmic contact made of a metal and an optical coating, beyond a partially-depleted highly-doped region. Moreover, a technique employed by many manufacturers to increase the ruggedness of the devices is to include a surface passivation layer of silicon oxide (SiO_2). If the dead layer is assumed to be made entirely of SiO_2, the numbers given above change to $(246 \pm 12 \pm 8)$ nm, i.e. the difference in the thickness of the dead layer is $\approx 4\%$. To avoid ambiguities, we refer to the result obtained assuming that the

material of the dead layer is pure silicon as the *silicon-equivalent thickness*.

ii. Wall et al. (2014) were able to show, through a detailed Monte Carlo simulation, that a part of the minority charge carriers generated by energy deposition in the dead layer does contribute to the signal by diffusion to the depleted region. Results with their model are presented in Section 6. Unfortunately, in the present case, the data do not have enough sensitivity to constrain both the fraction of the minority charge carriers that is recovered from the dead layer and its thickness. The minimum of χ^2 analysis discussed in Section 6 gives a silicon-equivalent thickness of (327 ± 2) nm, when no minority charge carrier is recovered from the dead layer, and of (498 ± 3) nm, when half of the generated minority charge carriers are recovered from the dead layer, see Section 6.3. Note once more that the uncertainty given is statistical only and does not cover the difficulties of accurately modelling the energy deposition or the incomplete charge collection. As discussed in Section 5.6, there is a strong indication that diffusion is important in the detector, since it is possible to see a spectrum even with no applied bias. Therefore, it is highly likely (but not fully proven by the present data) that the dead layer thicknesses, obtained in the CSDA approximation or with Monte Carlo simulations under the assumption that no minority charge carriers can be recovered from it, are not realistic and a more correct estimate is the value given above resulting from simulations where half of the minority charge carriers is assumed to contribute to the signal. Finally, it is worth recalling that while Wall et al. (2014) needed to know very precisely the value of the dead layer to attempt to determine the neutrino mass with an accuracy better than 0.2 eV from the spectrum of the β^- decay of tritium, the intended application here is to measure the energy of the electrons deflected by thin metallic foils to test multiple-scattering theories. Moreover, in the present setup, the average effect of the dead layer can be taken into account by resorting, for routine use unlike done here, to an energy calibration based on an independent determination of the beam energy employing the photons from the bremsstrahlung tip.

5.6. Evolution of the parameters with bias voltage

To conclude the experimental investigation of the RF, it is necessary to study the behaviour with the applied bias. The following four phenomena are sensitive to the reverse polarisation voltage.

i. The thickness of the depleted region increases with reverse voltage, as found in paper I, resulting in a larger active zone.

ii. The charge collection also improves with a higher bias and the associated fluctuations, i.e. σ_{cc} in Eq. (5), decrease (Owens, 1985). However, it is important to remember that, even exceeding the maximum safe rating recommended by the manufacturer (20 V), no evidence of full depletion has been found for the BPX 65 at reverse voltages up to 25 V in paper I. Therefore, it is not possible to apply high electric field strengths to the depleted and intrinsic regions by operating beyond full depletion, as commonly done in commercial high-purity devices meant to be used as particle detectors. As a consequence, diffusion of the charge carriers still has an important role for the results discussed here.

iii. A larger thickness of the depleted region reduces the depleted-region capacitance C_T resulting in a decrease of several contributions to the electronic noise, i.e. σ_{el} in Eq. (5), see e.g. the detailed analysis reported by Weinheimer et al. (1992).

iv. The increase in bias also leads to a higher reverse current and therefore a larger associated contribution to the electronic noise, i.e. σ_{el} in Eq. (5), see e.g. again the article by Weinheimer et al. (1992).

As found, e.g. by Bueno et al. (1996, 2004), items *iii* and *iv* have

opposite tendencies and can result in an optimum bias that leads to a minimum electronic noise.

A set of spectra has been measured for reverse biases from 0 to 30 V, and they have been analysed by subtracting the background, see Section 5.1, and then fitting the parameters of the expression presented in Section 5.2 with the method discussed in Section 5.3. The average beam energy has been set at (59.515 ± 0.003) keV, below the ≈ 85 keV that corresponds to electrons whose CSDA range is equal to the thickness of the depleted and intrinsic regions of (60 ± 3) μm at 18 V. The parameters

fitted to the experimental RF are plotted against the applied voltage in Fig. 5, which corresponds to Fig. 4 panel by panel: the 4 non-linear ones, i.e. σ (converted to FWHM), d, C and E_0 are displayed in panels (a), (b), (c), and (d), respectively, and the 3 linear ones, i.e. N_1, N_2, and N_3, in panel (e). For panels (a), (b), and (d), the information could have been, more correctly, reported in channels but, since the photodiode is intended to be employed as a particle detector, it has been converted to energy using the calibration discussed in Section 5.5, which is, strictly, appropriate only for the bias of the working point of 18 V. Relative
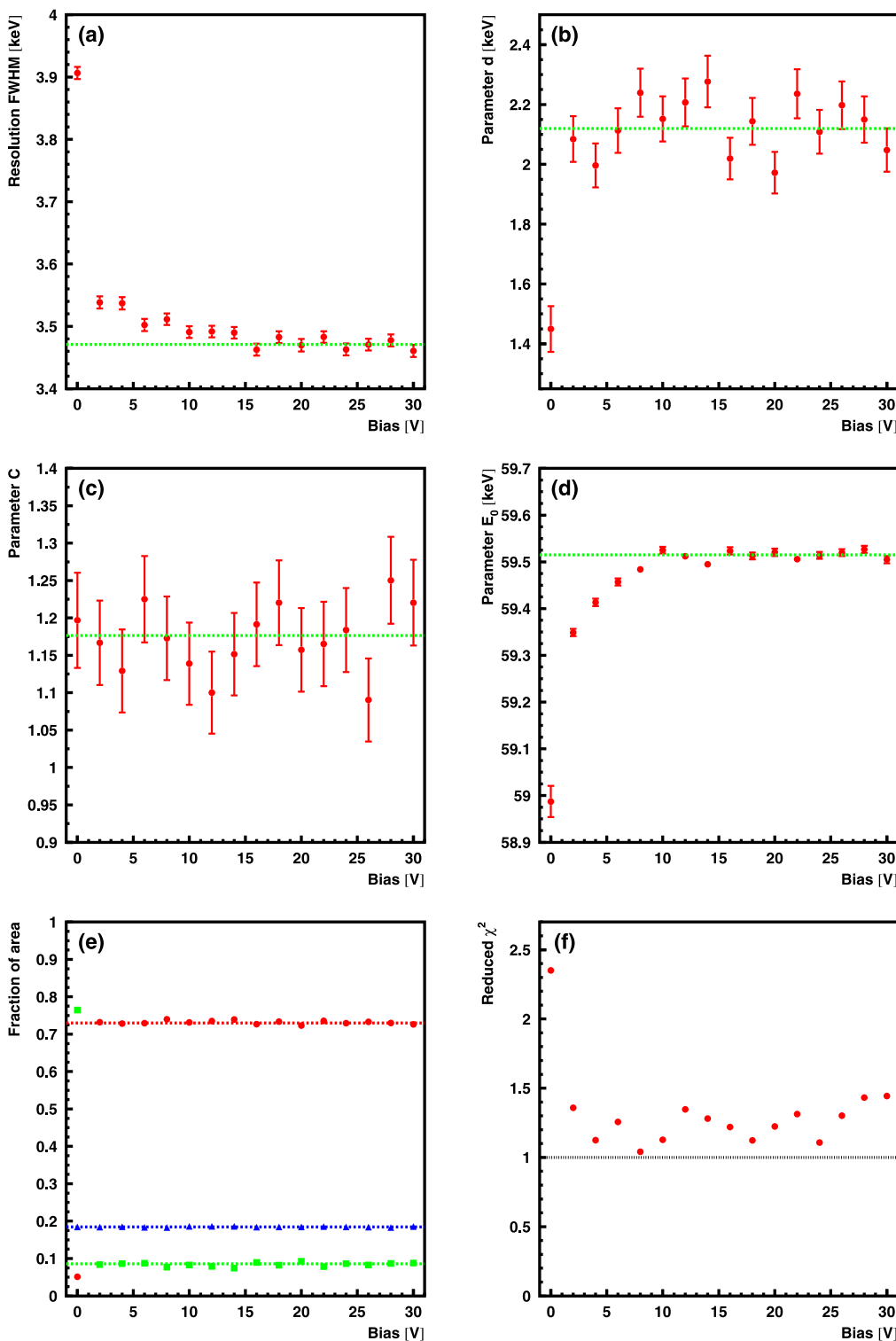

Fig. 5. Behaviour of the parameters of the RF model proposed here (see Subsection 5.2 or Appendix A) with the applied reverse bias for a monoenergetic beam of electrons with an average energy of (59.515 ± 0.003) keV. The 4 non-linear parameters, i.e. σ, d, C, and E_0 (see Eqs. (3) and (6) or Appendix A), are shown in panels (a), (b), (c), and (d), respectively. The 3 linear ones, i.e. N_1, N_2, and N_3, which are the normalisations of the contributions 1 (FEP), 2 (asymmetric tail on the lower side of the FEP), and 3 (LET), are displayed in panel (e) with red bullets, green filled squares, and blue filled triangles, respectively. Finally, the reduced χ^2 of the fit is plotted in panel (f). The green dashed horizontal lines in panels (a), (b), (c), and (d) indicate the average, weighted with the statistical uncertainties of the points, considering only those at a reverse bias of 18 V and above. The dashed horizontal lines in panel (e) have the same meaning for the series of points with the same colour. (For interpretation of the references to colour in this figure legend, the reader is referred to the Web version of this article.)

variations of the parameters shown in those panels are, of course, not affected by such a choice. Finally, the reduced χ^2 of the fit is reproduced in panel (f). As in Fig. 4, the uncertainty bars are statistical only and correspond to one standard deviation (see Appendix B for more details on the fitting procedure and on how the uncertainties are estimated).

The evolution of the resolution, converted to FWHM, is displayed in Fig. 5 (a). The green dashed horizontal line represents the average, weighted with the statistical uncertainties of the points, considering only those at 18 V and above. The initial improvement with the increase in reverse bias is clear but there is no sign of a minimum, as also found in paper I. As discussed there, the reverse current of the samples of BPX 65 tested is ≈ 0.1 nA at 20 V, approximately one order of magnitude lower than the maximum rating given by the manufacturer. For such a value and a formation time of 2 μs (see Section 2), the associated white noise contributes to the resolution with 410 eV FWHM (Weinheimer et al., 1992). Therefore, when added quadratically to the other electronic noise sources, it is not important and does not lead to an overall worsening at higher reverse voltages.

The charge-collection efficiency can be monitored by the parameter d in Eq. (3), i.e. the energy scale of the exponential present in contribution 2, see Fig. 5 (b). The green dashed horizontal line has the same meaning as in panel (a). As long as some bias is applied, the parameter d rapidly attains its constant value, within the estimated uncertainties, and it is not affected by any further voltage increase. In quite general terms, the charge-collection efficiency is expected to improve with reverse bias, but this effect is more evident for E_0, see below. The presence of a clear FEP even at 0 V indicates the importance of diffusion of the charge carriers for the generation of the signal in the BPX 65. For no polarisation, beyond the FEP with an asymmetric tail on the lower side and the LET, another feature appears in the spectrum: a tail close to the threshold of the discriminator extending to ≈ 5 keV above it. This is yet another evidence of a worse charge-collection efficiency when the external field is not strong enough. Such a part has been excluded from the fit of the RF. It is absent for biases above ≈ 10 V. Problems with charge collection have also been observed below ≈ 8 V with photons in paper I.

The position of the maximum in the LET, controlled by the parameter C appearing in Eq. (6), does not show any evolution with bias, within the estimated uncertainties, as displayed in Fig. 5 (c). The green dashed horizontal line has the same meaning as in panels (a) and (b). This is another clue that this part of the RF is connected with the energy distribution of the backscattered electrons, as shown by Planskoy (1968), see Sections 4.1, 5.4, and 6, and not with incomplete charge collection, which, on the contrary, depends on the bias.

Again, as in paper I, the charge-collection efficiency can also be studied by analysing the position of the FEP, i.e. the parameter E_0 in Eqs. (3) and (6), as a function of the reverse bias, see Fig. 5 (d). Since the variation is big, the nominal beam energy has not been subtracted as in Fig. 4 (d). The green dashed horizontal line has the same meaning as in panels (a), (b), and (c). A partial loss of the generated charge is clearly visible and only above ≈ 10 V the position of the FEP reaches its asymptotic value and does not change further. A similar result has been found in paper I with photons. The electrons loose energy as soon as they enter the detector, therefore the disappearance of the generated charge can be due to a deposition outside the depleted and intrinsic regions (the quoted value of (60 ± 3) μm refers to 18 V) or to diffusion and recombination. The impact of both effects is diminished with a higher bias. It is important to remember that electrons suffer elastic scattering and their tracks are not straight, thus depositing the energy at depths smaller than the CSDA range. Moreover, a part of the energy deposited in partially-depleted regions can also contribute to the signal by diffusion of the minority charge carriers, as found by Wall et al. (2014) and Zhao et al. (2016). It is the net balance of all these contributions what determines the exact shape of Fig. 5 (d).

As in Fig. 4 (e), the fractions of the area of the RF associated to each

of the contributions, i.e. $N_1/(N_1 + N_2 + N_3)$, $N_2/(N_1 + N_2 + N_3)$, and $N_3/(N_1 + N_2 + N_3)$, are shown in Fig. 5 (e) with red bullets, green filled squares, and blue filled triangles, respectively. The horizontal dashed lines represent the average, weighted with the statistical uncertainties of the points with the same colour, considering only those at 18 V and above. The trends agree with those already discussed. The fraction of the area in the asymmetric contribution to the FEP decreases as soon as some bias is applied, accompanying the evolution of the parameter d discussed in connection with Fig. 5 (b). The complementary fraction of the area in the FEP changes, of course, in the opposite direction. The fraction of the area in the LET does not depend on the polarisation voltage, following the behaviour of the parameter C discussed in connection with Fig. 5 (c).

Finally, the quality of the fits is illustrated by plotting the evolution of the reduced χ^2 in Fig. 5 (f). Except for 0 V, where the shape of the RF is deformed by incomplete charge collection, all other values remain below ≈ 1.4, indicating a reasonable overall agreement with no visible trend.

6. Comparison with Monte Carlo simulations

Developing a special-purpose Monte Carlo code is a large effort which is not justified for the present scope. Here we prefer to employ general-purpose Monte Carlo codes, but a choice has to be made considering the accuracy of the description of the interaction of low-energy electrons with matter. Then an incomplete charge-collection model, which is not typically part of a general-purpose package, has to be implemented before comparing with data.

6.1. Choice of a simulation tool

An accurate Monte Carlo simulation of the interaction of low-energy electrons with matter requires the inclusion of the following processes.

i. Elastic scattering of the electrons by the screened Coulomb field of the atoms of the medium. This mechanism does not contribute directly to the energy loss, but changes the direction of propagation of the electrons and is therefore essential to correctly reproduce, e.g., backscattering that can result in the escape of particles from the active part of the detector.

ii. Inelastic collisions. They can excite or ionise the atom, see *iii*, resulting in an energy loss of the impinging electron.

iii. Generation of secondary electrons by ionisation. In some of the inelastic collisions, the atom is ionised and the ejected electron can have sufficient energy to travel distances comparable to the dimensions of the internal structures of the device. Therefore, not all the energy lost by the impinging electron is deposited locally. This is important especially close to the dead layer or to the detector border, since it can result in an inelastic collision of an electron, e.g. in the dead layer, that deposits energy in the active volume and vice versa. This kind of cross talk has been emphasized by Goto (1993, 1998), Chaoui et al. (2009), Chaoui and Renschler (2010), and Renschler (2011). The philosophy behind the detailed description of ionising collisions is that, of course, all secondary electrons, called δ-rays in the older literature, must be followed in the same detailed way as the primary one.

iv. Decay of excited atoms by Auger cascades, fluorescence, or shake-off. As in the previous item, all these processes, which take place to restore an atom to its ground state after excitation by an ionising collision, can transport the energy lost by the impinging electron over distances larger than the dimensions of the internal structures of the device. For silicon, the dominating process is by far an Auger cascade with the emission of one or more secondary Auger electrons.

v. Bremsstrahlung emission. This energy-loss process plays a minor role in silicon owing to the low atomic number of this element as

well as to the low energies of the electrons involved and reduced dimensions of the studied device.

Typical mean free paths for elastic or inelastic collisions of electrons with a few tens of keV in solid media are of the order of 1 μm or less, thus resulting in a large number of collisions to be simulated. If inelastic collisions are to be treated in a detailed way, all secondary electrons must be followed, increasing the number of particles to be tracked. To simplify this, even nowadays, computer intensive task, first-generation simulation codes, like the mentioned pioneering work by Berger et al. (1969), used the Goudsmit–Saunderson multiple-scattering theory and the Bethe formula to group together the effect of several elastic and inelastic collisions, respectively. Second-generation codes, like those by Schüpferling (1975) or Frommhold et al. (1991), treated in a detailed way elastic collisions only, adopting different kinds of approximations for the basic cross sections (Goto (1993, 1998), who was interested in photons, also did so). To avoid the extra computational cost of following a large number of secondary electrons, several inelastic collisions were still grouped together and treated in a condensed way by using the Bethe formula. Finally, modern third-generation codes, like that written by Chaoui et al. (2009) and employed within the KATRIN collaboration, simulate each individual ionising collision and the subsequent decay of the ionised atom, taking into account all secondary electrons explicitly, whose interaction histories are, in turn, followed. It should be clear that the proposed subdivision in generations is schematic; indeed, the evolution from one to the next is mostly driven by the availability of increasing computing power and is not simply related to the quality of the results: with badly approximated cross sections even a fully detailed description can give inaccurate results.

Two of the best general-purpose Monte Carlo codes are PENELOPE (Baró et al., 1995; Sempau et al., 1997; Salvat, 2015, 2019) and Geant4 (Agostinelli et al., 2003). As reported by Renschler (2011), Geant4, at least up to version 4.9.1, suffered from a strong dependence of the energy-loss spectrum in thin dead layers from the choice of the tracking parameters (see e.g. Fig. 4.2 by Renschler (2011)) and has therefore been avoided.

The other natural choice is to employ PENELOPE version 2018 (Salvat, 2019), the latest at the moment of submission of the present paper. Beyond its refined description of the basic cross sections, it has the additional advantage of a transport mechanics which can be switched from condensed to detailed depending on the tracking parameters. The implementation of items *i* to *iv* above is as follows.

The elastic cross sections adopted for *i* are those prepared by Salvat with the ELSEPA code (Salvat et al., 2005). They are distributed in the form of digital tables in two ways: one together with the ICRU Report 77 (Berger et al., 2007) and the other as the NIST Standard Reference Database Number 64 (Jablonski et al., 2016). They are based on a Dirac partial-wave calculation in a central potential, whose static part is obtained with a Dirac–Fock self-consistent procedure. A correction term for exchange effects is also included. They are essentially the best elastic cross sections computed in systematic form and made publicly available, and they were employed by Chaoui et al. (2009) as well. In this respect, what is done here is very close to what was implemented by Chaoui and collaborators (Chaoui et al., 2009; Chaoui and Azli, 2010; Chaoui and Renschler, 2010; Chaoui and Goto, 2010; Renschler, 2011; Wall et al., 2014).

The inelastic cross sections for *ii* are obtained from the plane-wave Born approximation (PWBA), which in turn needs a Generalised Oscillator Strength (GOS) for each atomic shell. The simplified Sternheimer–Liljequist GOS model is adopted since it requires only three parameters: the number of electrons in the shell, the binding energy of the shell and the mean excitation energy of the material. The latter is selected so that the electronic stopping power closely agrees with the values from ICRU Report 37 (Berger et al., 1984). Unfortunately, the simplified GOS model produces artefacts for the energy loss in thin layers. Indeed they have been observed e.g. by Renschler (2011), see his

Fig. 4.3, referring to PENELOPE version 2008. The situation has prompted further modifications in more recent versions of PENELOPE (see Section 3.2.2.1 of the manual (Salvat, 2019)).

The ionisation cross sections of inner shells (i.e. K, L_1, L_2, and L_3 for silicon) for *iii* are taken from extensive tabulations calculated with the distorted-wave Born approximation (DWBA) as formulated by Bote and Salvat (2008). They are publicly available as the NIST Standard Reference Database Number 164 (Llovet et al., 2014). The cross sections for the outer shells (i.e. M_1 and M_2 for silicon) are still obtained from the PWBA with the Sternheimer–Liljequist GOS model, but they are corrected to compensate for the difference between the cross sections obtained in the DWBA and the PWBA for inner shells to yield an electronic stopping power in agreement with the ICRU Report 37 (see Section 3.2.6.1 of the manual (Salvat, 2019) or the description of recent improvements by Salvat (2015)). Chaoui et al. (2009) used Penn's dielectric function formalism (Penn, 1987) to calculate inelastic collisions including plasmon excitations, interband transitions, and inner-shell ionisations (for details, see the articles cited by Chaoui et al. (2009)). This is possible for silicon since it is a very well-known material and all the parameters of the dielectric function for optical photons are readily available. In their case, all inelastic collisions result in the emission of secondary electrons, which are propagated down to 1 eV. To assign the inelastic collision to a shell, the process is described as the exchange of a virtual photon and the same relative probabilities for absorption of a real photon, taken from the tabulation by Cromer and Liberman (1970), are assumed (Chaoui et al., 2009). The Sternheimer–Liljequist GOS model, even as updated in the more recent versions of PENELOPE, is still too simplistic to describe accurately the energy-loss distribution when the electron undergoes few inelastic collisions. Nevertheless, the first two moments of the distribution are correct. In this respect, Penn's dielectric function model is superior (e.g. Chaoui and Renschler (2010) have shown results where the loss in a thin dead layer include even the structures due to excitation of surface plasmons) but its complexity has precluded implementation in general-purpose Monte Carlo codes. In conclusion, the main difference between the present calculations and those published by Chaoui et al. (2009), Chaoui and Azli (2010), Chaoui and Renschler (2010), Chaoui and Goto (2010), Renschler (2011), and Wall et al. (2014) is the description of inelastic collisions.

The cascade of Auger electrons in the decay of ionised atoms for *iv* are simulated in PENELOPE according to the transition probabilities tabulated in the Evaluated Atomic Data Library by Perkins et al. (1991). Chaoui et al. (2009), Chaoui and Azli (2010), Chaoui and Renschler (2010), Chaoui and Goto (2010), Renschler (2011) and Wall et al. (2014) used instead the values by Fraser et al. (1994). A study of the effect of the emission of Auger electrons on the energy spectra of the electrons that leave the surface of a silicon detector has been published by Chaoui and Goto (2010).

Benchmarks of the PENELOPE Monte Carlo code by comparison with measurements of the fraction of electrons and positrons backscattered from bulk samples and their energy and angular distributions as well as of the fraction of electrons transmitted through thin metallic foils and their energy distributions have been published by Benedito et al. (2001) and Sempau et al. (2003). The agreement is in general good. The code by Chaoui and co-workers has been compared to recent high-resolution experimental energy distributions of electrons backscattered from silicon finding an overall good agreement (Chaoui et al., 2009; Chaoui and Azli, 2010).

For the results presented here, the simulated number of primary electrons is $2 \cdot 10^6$, requiring ≈ 10 h of CPU time for the worst case of primary electrons with an energy of 100.03 keV again on a computer with a 64-bit CPU running at 2.0 GHz (opteron 6128 HE manufactured by AMD®). All the absorption cuts have been set to 50 eV. The tracking cuts C_1, C_2, W_{CC}, and W_{CR} have been set to zero resulting in fully detailed simulations of both elastic and inelastic collisions. For such a reason, the methods used to group several soft elastic or inelastic

collisions, that are implemented in PENELOPE and can be enabled, selecting non-zero values of C_1, C_2, W_{CC}, and W_{CR}, to speed up the simulations, have not been described here. However, the interested reader can find the corresponding information in the publication by Benedito et al. (2001) and in the manual (Salvat, 2019).

6.2. Incomplete charge-collection model

Once a rather accurate detailed description of the interactions of electrons in silicon is available, several authors have called the attention on the need to model the charge-collection properties of the device (Goto, 1993, 1998; Hartmann et al., 1996; Renschler, 2011; Iwamoto et al., 2011; Wall et al., 2014). If the doping profiles are known, or can be measured with Secondary Ion Mass Spectrometry (SIMS) by sacrificing one sample, like done by Hartmann et al. (1996), simulation packages usually employed by the microelectronic industry can supply this information. This is not the case of the BPX 65, as mentioned, and it is necessary to resort to generic and, of course, more approximate descriptions.

The geometrical structure of the BPX 65 is that of a parallelepiped with a square 1 mm × 1 mm face and a thickness much larger than the anticipated CSDA range of the highest energy electrons considered in the present study. It has been set to a reasonable value of 300 μm in the simulations. Of these, only the first 60 μm correspond to the depleted and intrinsic regions according to the capacitance measurements discussed in paper I. They have been implemented in the geometry-definition file of PENELOPE/penEasy (Salvat, 2019) as two separate volumes, of which only the first, closest to the entrance face and with a thickness of 60 μm, is considered active (i.e. subject to scoring of the deposited energy). If the entrance face of the detector is in the xy plane, the perpendicular z direction describes the depth inside it (here the convention is that the entrance face of the detector is located at $z = 0$ and the end face of the depleted and intrinsic regions at $z = z_a = 60$ μm). The simple charge-collection models discussed in the literature (Goto, 1993, 1998; Wall et al., 2014) neglect the effect of the borders of the detector in the x and y directions and are therefore described by an appropriate weighting function $C(z)$ that gives the energy signal E_{det} as a function of the energy deposited E_{dep} by the primary or any of the secondary electrons according to

$$E_{det} = \sum_i E_{dep}(z_i) \, C(z_i) \qquad , \qquad (7)$$

where the sum runs over all the tracking steps in which energy has been deposited at positions z_i during one complete Monte Carlo history (Eq. (7) is applied, of course, event-by-event). Complete charge collection is described by $C(z) = 1$ for $z \in (0, z_a)$.

Because of the metallic ohmic contact, the optical coating, and a partially-depleted highly-doped region, there is an entrance dead layer to the depleted and intrinsic regions. The most basic treatment is to assume that in these three structures no signal can be collected. Wall et al. (2014) generalised such an approach by taking into account the effect of diffusion of the minority charge carriers generated in the dead layer to the depleted and intrinsic regions. In the simplest approximation, a fraction f_W of the energy deposited becomes visible

$$C_W(z) = f_W + (1 - f_W) \, \Theta(z - z_W) \quad , \qquad (8)$$

where the thickness of this partially-dead layer is indicated as z_W. A totally dead layer is a special case of Eq. (8) where $f_W = 0$. Very good agreement with measured spectra was achieved by Wall et al. (2014) when a fraction of 46% of the minority charge carriers produced in the dead layer was assumed to contribute to the signal. This value is very close to that expected from random diffusion, where half of the minority carriers migrate towards the contact and are neutralised and half to the depleted region and contribute to the signal. However, the effect of diffusion and recombination of the charge carriers produced in the

intrinsic and depleted regions, which is possibly important in the BPX 65 as mentioned in Section 5.6, is not accounted for. The role of diffusion in over-depleted Si(Li) diodes was studied by Goto (1993, 1998), whose approach is not adequate here since it assumes a homogeneous condition inside the detector where the relative importance of drift and diffusion is constant. Thus, a complete description is missing. Eq. (8) is a reasonable approximation if there are well-separated high- and low-field regions, where the dominant contributions to the transport of the charge carriers are drift and diffusion, respectively. As mentioned also in paper I, Zhao et al. (2016) conducted absolute efficiency measurements on their devices for 5.9-keV photons with a calibrated radioactive source and found values that were higher than what would be expected by considering only the solid angle and the probability of interaction in the active volume. They also attributed their results to minority charge carriers generated in the undepleted or partially depleted regions reaching by diffusion the depleted one (which in their case had a thickness of few microns). We stress that such an effect has a smaller impact for photons, which interact at randomly-distributed points, than for electrons, which start to loose energy as soon as they impact on the detector front face.

Eq. (8) has been chosen, following Wall et al. (2014), since it depends on two parameters, z_W and f_W, which can be determined by scanning the physically acceptable space and comparing Monte Carlo simulations to data. This is particularly relevant for a commercial device, whose construction details are unknown. Eq. (8) has been implemented in a modified version of the penEasy main program. The effect of electronic noise is taken into account by smearing the collected energy signal from Eq. (7) with a Gaussian distribution, whose FWHM is 3.371 keV, which is the value obtained by the fit of the parameters of the RF discussed in Section 5.4, averaged over the energies of the impinging electrons covered here.

6.3. Comparison with data

An analysis of the minimum of χ^2 (Brandt, 2014) has been performed to determine the free parameters of the model considering simultaneously all the measurements at the $n^{exp} = 9$ different beam energies from 10.39 keV to 80.18 keV. Energies of 84.99 keV and above have been excluded because the CSDA range of the impinging electrons is equal to or greater than the thickness of the depleted and intrinsic regions of (60 ± 3) μm at 18 V. In detail, the value to be studied is

$$\chi^2 = \sum_{i=1}^{n^{exp}} \sum_{j=1}^{n_i} \frac{\left(c_i^{MC} n_{i,j}^{MC} - c_i^{exp} n_{i,j}^{exp}\right)^2}{\left(\sigma_{i,j}^{exp}\right)^2 + \left(\sigma_{i,j}^{MC}\right)^2} \qquad , \qquad (9)$$

where the indexes $i = 1, \ldots, n^{exp}$ and $j = 1, \ldots, n_i$ run over the n^{exp} sets of data and the channels in each set, respectively. The content of the j-th channel in the i-th set in the measurement and in the corresponding simulation are represented by $n_{i,j}^{exp}$ and $n_{i,j}^{MC}$, and their uncertainties (defined as one standard deviation in the present work) by $\sigma_{i,j}^{exp}$ and $\sigma_{i,j}^{MC}$, respectively. Since the energy corresponding to the centre of each channel in the experiment depends on the energy calibration and is, therefore, a broken number, the simulations have been run with more bins and the values of $n_{i,j}^{MC}$ and $\sigma_{i,j}^{MC}$ obtained by a linear interpolation. Finally, because the total number of impinging electrons in the data cannot be measured (see Section 2), it is necessary to determine the normalisation factors c_i^{exp} and c_i^{MC}. To reduce numerical instabilities, initial guesses of c_i^{exp} and c_i^{MC} are supplied by setting the maximum channel content in the data and simulation to one, the values of $n_{i,j}^{exp}$ and $n_{i,j}^{MC}$ are updated (preserving the correct magnitude of the uncertainties) and c_i^{exp} is set to one. Then, an improved estimate of c_i^{MC} is obtained by solving the corresponding one dimensional Normal Equation (Brandt, 2014)

$$c_i^{\mathrm{MC}} = \frac{\sum_{j=1}^{n_i} \frac{n_{i,j}^{\exp} \, n_{i,j}^{\mathrm{MC}}}{\left(\sigma_{i,j}^{\exp}\right)^2 + \left(\sigma_{i,j}^{\mathrm{MC}}\right)^2}}{\sum_{j=1}^{n_i} \frac{n_{i,j}^{2\mathrm{MC}}}{\left(\sigma_{i,j}^{\exp}\right)^2 + \left(\sigma_{i,j}^{\mathrm{MC}}\right)^2}} \qquad . \tag{10}$$

Unfortunately, the measurements collected for the present work do not have the capability to fix simultaneously both f_W and z_W. Therefore, f_W is fixed first and then a full set of simulations run for a grid of 7 values of z_W from 100 nm to 700 nm in steps of 100 nm. The corresponding χ^2 is calculated according to Eqs. (9) and (10) and the minimum $\chi^2_{\min}$ found by fitting the parameters of a parabola, see Table 1. It is never enough to stress that the uncertainty on z_W given in Table 1, corresponding to a variation from $\chi^2_{\min}$ to $\chi^2_{\min} + 1$, is statistical only and does not include the inaccuracies of the model used to describe the data. For the best estimates of z_W given by $\chi^2_{\min}$, one final set of simulations has been run and a few selected results are shown in Fig. 6 for the same representative energies considered in Fig. 3. The case of a perfect charge-collection efficiency is also shown for comparison in Fig. 6.

The main features of the measurements are well reproduced by the simulations, but not the quantitative details as is also evident from the values of $\chi^2_{\min}$/n.d.f. presented in Table 1. The main conclusions that can be drawn from Table 1 and Fig. 6 are the following.

a. The relative areas of the FEP and the LET are not well reproduced at 100.03 keV. Because the absolute normalisation is not known in the data, the comparison shown in Fig. 6 is only relative and it is not possible to disentangle which of the two contributions is not correctly described in the simulations. The problem actually becomes visible at 90.21 keV and worsens with increasing energy. In the present simulations, the active layer of the detector has exactly the thickness of the depleted and intrinsic regions determined by the measurements of the junction capacitance described in paper I. However, if part of the minority charge carriers generated in the front dead layer diffuses to the active region and contributes to the signal, it is also possible that part of the minority charge carriers produced in the undepleted region at the back of the device can diffuse to the active region and contribute to the signal. Evidences of such a process have indeed been found for light ions, which suffer much less multiple scattering, impinging on several types of semiconductor detectors (Vittone et al., 1999; Manfredotti et al., 2001; De Napoli et al., 2009; Iwamoto et al., 2011). Correspondingly, generalisations of Eq. (8) have been proposed (Breese, 1993; Breese et al., 2007). However, they require knowledge of the transport parameters of the charge carriers, most importantly their diffusion lengths, which cannot be determined reliably for a commercial device whose construction details are not known. Such a path has not been followed in the present work. The importance of these effects starts at

energies for which the CSDA range is larger than the thickness of the depleted and intrinsic regions and increase thereafter, similarly to what is observed in the comparison to the data. For this reason, the analysis of the minimum of χ^2 shown in Table 1 has been limited to beam energies for which the CSDA range of the impinging electrons is smaller than the thickness of the depleted and intrinsic regions of (60 ± 3) μm at 18 V. As a matter of fact, a sharp increase in the $\chi^2_{\min}$/n.d.f. is observed when energies of 84.99 keV or above are included in the analysis.

b. The shape of the LET is very well reproduced at all energies: this would be even more clearly evident if a normalisation in the LET region alone would be applied. The area of the LET is, as mentioned in the item above, well reproduced below 90.21 keV and there is no way to know if the mismatch at higher energies is due to the simulation of the LET itself or of the FEP. However, in the previous item, an argument has been offered to make it plausible that the origin of the problem above 90.21 keV is related to events possibly missing from the FEP. Thus, from the good agreement between data and simulations, it can be concluded that the most likely physical origin of the LET are electrons that backscatter from the silicon crystal of the PIN diode and therefore deposit only a part of their energy into it.

c. The exponential tail on the lower side of the FEP is not present in the simulations that do not take into account incomplete charge collection, see Fig. 6. On the contrary, when the model by Wall et al. (2014), Eq. (8), is implemented, the outcome is quite close to the measurements. This again suggests that the origin of the asymmetry in the FEP has indeed been correctly identified: i.e. energy straggling in a partially or totally dead layer. Unfortunately, the data do not have enough sensitivity to constrain the two parameters f_W and z_W by an analysis of the minimum of χ^2. Only once f_W has been chosen, z_W can be obtained. Both a completely dead layer ($f_W = 0$) and a partially dead layer from which one quarter ($f_W = 0.25$) or half ($f_W = 0.5$) of the produced minority charge carriers is recovered by random diffusion describe equally well the measurements: compare the red and green curves in Fig. 6 or the values of $\chi^2_{\min}$/n.d.f. in Table 1. Wall et al. (2014) could determine both f_W and z_W from a minimum of χ^2 analysis. However, it is important to note that a special configuration of magnetic and electric fields was employed in that work to reflect the electrons backscattered from the PIN diode into it, resulting in a LET of the RF mostly sensitive to incomplete charge collection, contrary to the present situation.

7. Conclusion

The present paper II completes the characterisation of a commercial PIN photodiode, type BPX 65, started in paper I with the electrical part and with applications to photon spectrometry. Here, the response function (RF) to electrons is investigated profiting from an accelerator beam with well-defined energies between 10 and 100 keV. In general, three contributions are always visible in the RF: a full-energy peak (FEP), a low-energy tail (LET) extending from the FEP down to the discriminator threshold, and an asymmetric tail on the lower side of the FEP. An empirical model has been proposed, improving previously published ones, and compared in detail to measurements. The evolution of the free parameters with impinging electron energy and reverse bias has been studied and found to be smooth, giving confidence on the predictive power of the model, when applied to energies or voltages not covered in the scan. Details are given in two appendices on the numerical implementation of the function and, in particular, on the fitting procedure that treats the linear parameters separately from the non-linear ones to improve the efficiency by directly solving the Normal Equations with a Cholesky decomposition without any need for iterations.

The behaviour of the parameters of the RF with energy and voltage as well as a comparison with simulations performed with PENELOPE/
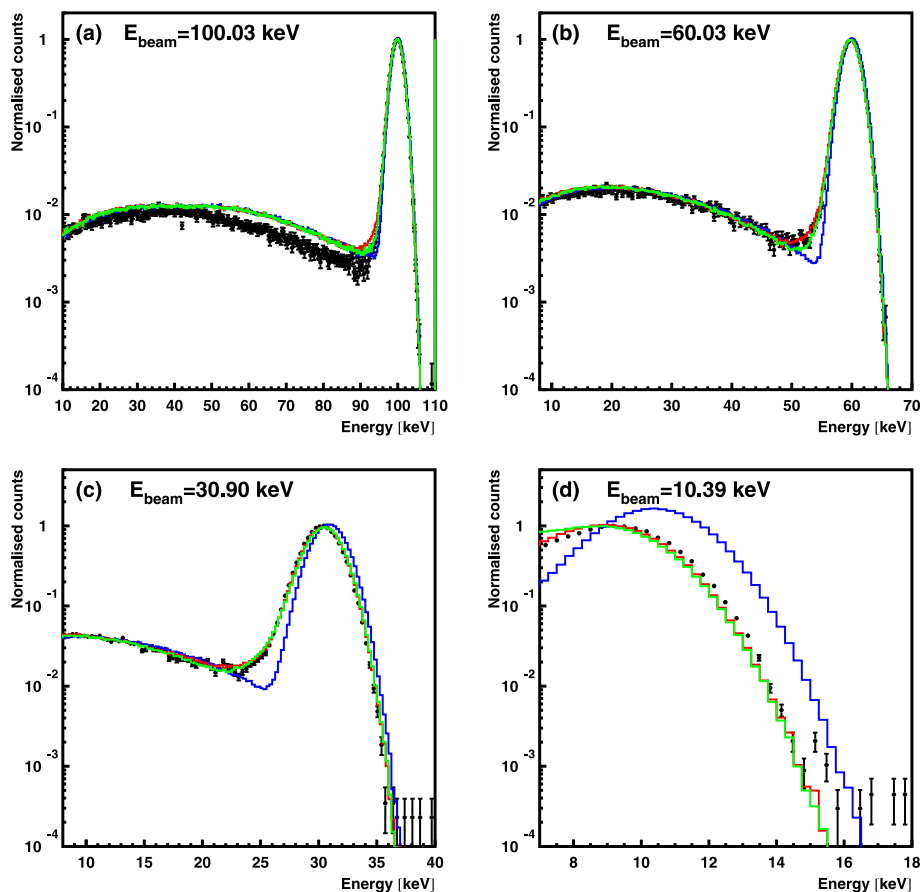
Table 1

Analysis of the minimum of χ^2 calculated according to Eqs. (9) and (10) for the incomplete charge-collection model proposed by Wall et al. (2014), see Eq. (8). Only beam energies from 10.39 keV to 80.18 keV have been considered because the CSDA range of the impinging electrons is less than the thickness of the depleted and intrinsic regions of (60 ± 3) μm at 18 V. The parameter f_W is fixed as indicated on the first leftmost column and the simulations are run on a grid of z_W points from 100 nm to 700 nm in steps of 100 nm. A fit of the parameters of a parabola to the values of χ^2 allows to estimate z_W and its statistical uncertainty (corresponding to one standard deviation), as given in the second column. The third column gives $\chi^2_{\min}$/n.d.f., the minimum of χ^2 normalised to the number of degrees of freedom n.d.f. $= 1133$.

f_W	z_W	$\chi^2_{\min}$/n.d.f.
	[nm]	
0	327 ± 2	6.6
0.25	395 ± 3	6.3
0.5	498 ± 3	6.5

Fig. 6. Comparison of the RF simulated with PENELOPE/penEasy to the spectra measured employing an electron beam with energies of 100.03 (a), 60.03 (b), 30.90 (c), and 10.39 keV (d). A complete charge-collection efficiency coupled to a Gaussian electronic noise does not reproduce the exponential tail on the low-energy side of the FEP (blue continuous curves). The main program penEasy has been modified to implement the incomplete charge-collection model proposed by Wall et al. (2014), see Eq. (8). The parameter f_W is fixed to 0 (red continuous curves) and 0.5 (green continuous curves), while z_W is derived from the analysis of the minimum of χ^2, see Eqs. (9) and (10), described in the text. The uncertainty bars, representing the statistical contribution alone, correspond to one standard deviation. The energy dispersion of the experimental and simulated histograms are 0.33 and 0.25 keV/-channel, respectively. (For interpretation of the references to colour in this figure legend, the reader is referred to the Web version of this article.)

penEasy allows to identify the physical origin of the three mentioned contributions to the RF.

The FEP is, of course, due to electrons whose interaction histories lead to complete deposition of their energy into the active volume of the detector. It is Gaussian with a FWHM of (3.371 ± 0.003) keV due to the experimental setup and the electronic chain employed. It matches well the value (3.30 ± 0.04) keV obtained with a pulser, which is somewhat worse than that reported in paper I owing to a larger electronic noise in the irradiation chamber of the accelerator. It is likely that the resolution observed for photons in the different setup of paper I could be reached with an improved electronic chain and a better electromagnetic screening. These values are quite comparable to those achievable with commercial PIN diodes operating at room temperature, but with the advantage of a hundred-fold reduction in cost.

The LET originates from electrons that backscatter from the silicon crystal of the PIN diode and therefore deposit only a part of their energy. This is an intrinsic feature of the silicon material and all detectors made of it will inevitably show a LET of the same magnitude for electrons within the energy range of the present work.

Finally, the asymmetry on the lower side of the FEP is due to energy-loss straggling (and possibly incomplete charge collection) in the entrance layers of the detector. Several arguments have been set forth indicating the importance of diffusion of charge carriers in the BPX 65, which cannot be operated in a fully-depleted or over-depleted condition, contrary to commercial high-purity devices. The asymmetry on the lower side of the FEP present in the data can be better described by simulations when the model of incomplete charge collection by Wall et al. (2014) is implemented, considering that there is a sharp transition between the low-field and the high-field regions, where diffusion and drift dominate, respectively. The silicon-equivalent thickness z_W of such a dead or partially dead layer depends on the assumed fraction of minority charge carriers f_W that can be recovered in the active volume: it is $z_W \approx 330$ nm for $f_W = 0$, which corresponds to a completely dead layer, and $z_W \approx 500$ nm for $f_W = 0.5$, which is the value expected considering that half of the minority charge carriers diffuse towards the contact and recombine, and half diffuse to the active region. This asymmetry on the lower side of the FEP is the only feature that can possibly be reduced in a commercial high-purity device by increasing the bias above full depletion. If the presence of this structure can be tolerated, the reduction in cost is substantial, especially for detectors intended to be operated in a harsh radiation environment close to the beam of an accelerator, where frequent replacements can be anticipated.

Declaration of competing interest

The authors declare that they have no known competing financial interests or personal relationships that could have appeared to influence the work reported in this paper.

Acknowledgements

Appendix A. Explicit expression of the response function

As discussed in Section 4.1, the RF has three contributions: 1) full-energy peak (FEP), 2) asymmetric tail on the lower side of the FEP, and 3) low-energy tail (LET). In the present work, terms 1 and 2 are described with a Dirac delta function and an exponential convolved with a Gaussian, respectively (see also the explanation given in Section 5.2). Note that, for physical reasons, the generated number of electron-hole pairs can never be negative before the convolution with the Gaussian representing the effect of fluctuations, see Section 4.3. Thus, the integration has to be limited between 0 (no deposited energy) and E_0 (deposition of the full beam energy) and not between $-\infty$ and E_0, as done e.g. by Schüpferling (1975), Clifford et al. (1984), Yamamoto et al. (1988), and He et al. (1990). The correct expression for a convolution between 0 and E_0 (Brandt, 2014) is therefore

$$h_i(E, E_0) = \int_0^{E_0} f_i(E', E_0) \, \frac{1}{\sqrt{2\,\pi}\,\sigma} \, e^{-\frac{(E-E')^2}{2\,\sigma^2}} \, dE' \, , \tag{A.1}$$

where $f_i(E, E_0)$ is the intrinsic contribution to the RF before the effect of the fluctuations and σ is the standard deviation of the Gaussian employed to model them.

For contribution 1, corresponding to the FEP, the intrinsic description $f_i(E, E_0)$ is a Dirac delta function

$$f_1(E, E_0) = \delta(E - E_0) \, , \tag{A.2}$$

and therefore, after convolution, see Eq. (A.1), this gives just the Gaussian FEP of the RF

$$h_1(E, E_0; \sigma) = \frac{1}{\sqrt{2\,\pi}\,\sigma} \, e^{-\frac{(E-E_0)^2}{2\,\sigma^2}} \, . \tag{A.3}$$

For contribution 2, corresponding to the asymmetric tail on the lower side of the FEP, the intrinsic model is a decreasing exponential, mainly representing incomplete charge collection, correctly normalised between 0 and E_0

$$f_2(E, E_0) = \frac{1}{d\,(1 - e^{-E_0/d})} \, e^{-\frac{E_0-E}{d}} \, \Theta(E_0 - E) \, , \tag{A.4}$$

where Θ is the Heaviside step function and d is the parameter controlling the slope of the exponential with a dimension of energy. After convolution, see Eq. (A.1), this gives

$$h_2(E, E_0; \sigma, d) = \frac{e^{\frac{\sigma^2 + 2\,d\,(E-E_0)}{2\,d^2}}}{d\,(1 - e^{-E_0/d})} \left[\text{erf}\left(\frac{\sigma^2 + d\,E}{\sqrt{2}\,\sigma\,d}\right) - \text{erf}\left(\frac{\sigma^2 + d\,(E - E_0)}{\sqrt{2}\,\sigma\,d}\right) \right] \, , \tag{A.5}$$

where erf is the error function (Abramowitz and Stegun, 1972). The main differences with the equation adopted by Schüpferling (1975) appear within a few σ from the low-energy end of the spectrum at $E = 0$, where the effect of the convolution from 0 to E_0 or from $-\infty$ to E_0 has a bigger impact. This is, under most circumstances, immaterial because it happens in a region below the discriminator threshold used to reduce the impact of excess electronic noise on the acquisition dead time. However, it should be noted that the integral in the interval $(-\infty, +\infty)$ of the expression employed by Schüpferling for h_2 is not one, most probably because f_2 was normalised in the interval $(0, E_0)$ but the convolution was evaluated in the interval $(-\infty, E_0)$. Eq. (A.5) is used in the present study since its integral in the interval $(-\infty, +\infty)$ is more consistently one, although it results in a small increase of the computational cost with respect to that by Schüpferling due to one extra evaluation of the error function. The error function is actually an intrinsic in Fortran 2008 and later versions. For earlier versions, it is actually immediate to replace the error function in Eq. (A.5) with the complementary error function (Abramowitz and Stegun, 1972), which can be calculated very efficiently by means of a Chebyshev approximation using the routine published by Press et al. (1992).

Finally, for contribution 3, corresponding to the LET, the original form proposed by Damkjaer (1982), Eq. (4), has been modified to eliminate one strongly correlated parameter, as explained in Section 5.2, arriving at the simpler expression

$$h_3(E, E_0; C, \alpha) = \frac{A_N(C, \alpha)}{E_0} \, \frac{1 - E/E_0}{1 + C \exp\left(-\frac{(E/E_0)^2}{\alpha}\right)} \, . \tag{A.6}$$

No convolution with the Gaussian is performed to avoid a great increase in complexity once the result cannot be expressed in closed analytical form. If the expressions for f_1 and f_2 are correctly normalised, since the Gaussian in Eq. (A.1) is also normalised, the final expressions for h_1 and h_2 are correctly normalised, as it can be verified. The situation is different for Eq. (A.6) where the evaluation of the normalisation $A_N(C, \alpha)$ is necessary. This is not possible by analytical means and it is therefore carried out numerically. To reach a precision of more than five digits in the evaluation of Eq. (A.6), the integration interval from $E = 0$ to $E = E_0$ is divided in two equal parts and a 10-point Gauss–Legendre quadrature, whose abscissae and weights can be found in the book by Abramowitz and Stegun (1972), is applied to each sub-interval. As a matter of fact, the shape of Eq. (A.6) is a function of C and α alone and depends on E_0 only through the rescaling of the energy as E/E_0. This means that the normalisation constant A_N is fixed by the values of the parameters C and α, and needs to be recalculated only if they are changed by the fitting procedure.

The final expression of the RF obtained by combining Eqs. (A.3), (A.5), and (A.6) is then

$$h(E, E_0; \sigma, d, C, \alpha, N_1, N_2, N_3) = N_1 \, h_1(E, E_0; \sigma) + N_2 \, h_2(E, E_0; \sigma, d) + N_3 \, h_3(E, E_0; C, \alpha) \tag{A.7}$$

where N_1, N_2, and N_3 are constants needed to adjust the areas of each component to the measured RF. It is desirable to extract from the fit the fraction

of the total area associated to each contribution, therefore it is important that h_1, h_2, and h_3 are correctly normalised to 1 to enable a much simpler estimation of the errors on N_1, N_2, and N_3 without the need to propagate the uncertainties on the parameters of the fit with their covariances. From Eq. (A.7) it is clear that the RF depends on 8 free parameters: 5 non-linear, E_0, σ, d, C, and α, and 3 linear, i.e. N_1, N_2, and N_3. However, as mentioned in Section 5.2, the value of α is fixed to 0.0351 as recommended by Damkjaer (1982), leaving for the fit 7 adjustable parameters: 4 non-linear, i.e. E_0, σ, d, and C, and 3 linear, i.e. N_1, N_2, and N_3.

Appendix B. Fitting procedure

The fit to the data of the parameters of the RF, see Eq. (A.7) in A, is a non-linear problem. In the present study, the MINUIT (James and Roos, 1975) software package has been used, through its interface to PAW (Brun et al., 1989), to find a minimum of χ^2, defined in the usual way for the Least-Mean-Square problem (Brandt, 2014). The subroutines developed in the present work employ the 64-bit floating point representation of real numbers, as demanded by MINUIT (James and Roos, 1975). For all the cases considered here, the combination of MIGRAD (James and Roos, 1975), to find the minimum of χ^2, and MINOS (James and Roos, 1975), to include the non-linearities in the estimates of the uncertainties (i.e. deviations of the function to be minimised from a parabolic shape around the minimum), has been selected.

The minimisation of a function is in general a problem that scales badly with the number of dimensions and can become very difficult. In particular, many evaluations of the χ^2 can be necessary. Hence, it is important to use an expression that can reach a good description of the data with the smallest possible number of parameters, as done here with Eq. (A.7) (see in particular the change from Eq. (4) to Eq. (6) discussed in Section 5.2). It is also possible to still improve the situation by realizing that of the 7 adjustable parameters, 3 are linear, namely the constants N_1, N_2, and N_3 needed to match the areas of each component to the measured RF. A linear minimisation problem has always a direct solution in terms of the Normal Equations (Brandt, 2014), that can be found with standard linear algebra techniques. Therefore, the non-linear minimisation routine, i.e. MINUIT, must only take care of the 4 non-linear parameters, instead of the total number of 7, effectively reducing the computational complexity of the problem. The Normal Equations for the Least-Mean-Square problem actually result in a linear system whose matrix of the coefficients is symmetric and positive defined, which can be solved efficiently through the Cholesky decomposition (Press et al., 1992). However, because such a procedure is essentially a version of the Gaussian elimination without pivoting highly optimised for a symmetric and positive defined matrix, the non-dimensional form of the Normal Equations can improve the numerical stability. The Normal Equations

$$\boldsymbol{A} \cdot \boldsymbol{x} = \boldsymbol{b} \tag{B.1}$$

assume the following non-dimensional form

$$\boldsymbol{A}_{k,l} = \frac{S_{k,l}^2}{\sqrt{S_k^2\,S_l^2}}$$

$$\boldsymbol{b}_k = \frac{1}{\sqrt{S_k^2}} \sum_i \frac{h_k(E_i)\,n_i}{\sigma_i^2} \tag{B.2}$$

with

$$S_k^2 = \sum_i \frac{h_k^2(E_i)}{\sigma_i^2}$$

$$S_l^2 = \sum_i \frac{h_l^2(E_i)}{\sigma_i^2} \tag{B.3}$$

$$S_{k,l}^2 = \sum_i \frac{h_k(E_i)\,h_l(E_i)}{\sigma_i^2}\,,$$

where h_1, h_2, and h_3 are the three components of the RF as given by Eqs. (A.3), (A.5), and (A.6), respectively, and E_i, n_i, and σ_i are the centre of the channel of the measured histogram to be fitted, the channel content, and its uncertainty, respectively. The linear parameters N_1, N_2, and N_3 and their uncertainties $\sigma(N_1)$, $\sigma(N_2)$, and $\sigma(N_3)$ are given in terms of the solution of system (B.1) and the inverse of the matrix of the coefficients A^{-1} as

$$N_k = \frac{x_k}{S_k^2}$$

$$\sigma(N_k) = \frac{\sqrt{A_{k,k}^{-1}}}{\sqrt{S_k^2}}\,. \tag{B.4}$$

As a matter of fact, the Cholesky decomposition allows to obtain the inverse of the matrix of the coefficients efficiently (Press et al., 1992). The particular routine employed in the present work is the one given in the book by Press et al. (1992), after conversion to double precision.

Appendix C. Supplementary data

Supplementary data to this article can be found online at https://doi.org/10.1016/j.radphyschem.2020.109102.

References

Abramowitz, M., Stegun, I.A., 1972. Handbook of Mathematical Functions with Formulas, Graphs and Mathematical Tables, ninth ed. Dover, New York, USA.

Agostinelli, S., Allison, J., Amako, K., Apostolakis, J., Araujo, H., Arce, P., Asai, M., Axen, D., Banerjee, S., Barrand, G., Behner, F., Bellagamba, L., Boudreau, J., Broglia, L., Brunengo, A., Burkhardt, H., Chauvie, S., Chuma, J., Chytracek, R., Cooperman, G., Cosmo, G., Degtyarenko, P., Dell'Acqua, A., Depaola, G., Dietrich, D., Enami, R., Feliciello, A., Ferguson, C., Fesefeld, H., Folger, G., Foppiano, F., Forti, A., Garelli, S., Giani, S., Giannitrapani, R., Gibin, D., Gómez Cadenas, J.J., González, I., Gracia Abril, G., Greeniaus, G., Greiner, W., Grichine, V., Grossheim, A., Guatelli, S., Gumplinger, P., Hamatsu, R., Hashimoto, K., Hasui, H., Heikkinen, A., Howard, A., Ivanchenko, V., Johnson, A., Jones, F.W., Kallenbacha, J., Kanaya, N., Kawabata, M., Kawabata, Y., Kawaguti, M., Kelner, S., Kent, P., Kimura, A., Kodama, T., Kokoulin, R., Kossov, M., Kurashige, H., Lamanna, E., Lampén, T., Lara, V., Lefebure, V., Lei, F., Liendl, M., Lockman, W., Longo, F., Magni, S., Maire, M., Medernach, E., Minamimoto, K., Mora de Freitas, P., Morita, Y., Murakami, K., Nagamatu, M., Nartallo, R., Nieminen, P., Nishimura, T., Ohtsubo, K., Okamura, M., O'Neale, S., Oohata, Y., Paech, K., Perl, J., Pfeiffer, A., Pia, M.G., Ranjard, F., Rybin, A., Sadilov, S., Di Salvo, E., Santin, G., Sasaki, T., Savvas, N., Sawada, Y., Scherer, S., Sei, S., Sirotenko, V., Smith, D., Starkov, N., Stoecker, H., Sulkimo, J., Takahata, M., Tanaka, S., Tcherniaev, E., Tehrani, E.S., Tropeano, M., Truscott, P., Uno, H., Urban, L., Urban, P., Verderi, M., Walkden, A., Wander, W., Weber, H., Wellisch, J.P., Wenaus, T., Williams, D.C., Wright, D., Yamada, T., Yoshida, H., Zschiesche, D., 2003. Geant 4 - a simulation toolkit. Nucl. Instrum. Methods Phys. Res. 506, 250–303.

Baró, J., Sempau, J., Fernández-Varea, J.M., Salvat, F., 1995. PENELOPE: an algorithm for Monte Carlo simulation of the penetration and energy loss of electrons and positrons in matter. Nucl. Instrum. Methods Phys. Res. B 100, 31–46.

Barros, S.F., Maidana, N.L., Fernández-Varea, J.M., Vanin, V.R., 2017. Full-energy peak efficiency of Si drift and Si(Li) detectors for photons with energies above the Si K binding energy. X Ray Spectrom. 46, 34–43.

Barros, S.F., Vanin, V.R., Maidana, N.L., Martins, M.N., García-Alvarez, J.A., Santos, O.C.B., Rodrigues, C.L., Koskinas, M.F., Fernández-Varea, J.M., 2018. Ionization cross sections of the Au L subshells by electron impact from the L^3 threshold to 100 keV. J. Phys. B 51, 025201.

Benedito, E., Fernández-Varea, J.M., Salvat, F., 2001. Mixed simulation of the multiple elastic scattering of electrons and positrons using partial-wave differential cross-sections. Nucl. Instrum. Methods Phys. Res. B 174, 91–110.

Berger, M.J., Coursey, J.S., Zucker, M.A., Chang, J., 2017. Stopping-Power & Range Tables for Electrons, Protons, and Helium Ions, NIST Standard Reference Database Number 124. National Institute of Standards and Technology, Gaithersburg MD, p. 20899. https://doi.org/10.18434/T4NC7P.

Berger, M.J., Inokuti, M., Anderson, H.H., Bichsel, H., Dennis, J.A., Powers, D., Seltzer, S.M., Turner, J.E., 1984. Report 37: stopping powers for electrons and positrons. J Int Comm Radiat Units Meas os19, 1984.

Berger, M.J., Jablonski, A., Broníc, I.K., Mitroy, J., Powell, C.J., Salvat, F., Sanche, L., 2007. Report 77: elastic scattering of electrons and positrons. J Int Comm Radiat Units Meas 7, 2007.

Berger, M.J., Seltzer, S.M., Chappell, S.E., Humphreys, J.C., Motz, J.W., 1969. Response of silicon detectors to monoenergetic electrons with energies between 0.15 and 5.0 MeV. Nucl. Instrum. Methods 69, 181–193.

Bote, D., Salvat, F., 2008. Calculations of inner-shell ionization by electron impact with the distorted-wave and plane-wave born approximations. Phys. Rev. 77, 042701.

Brandt, S., 2014. Data Analysis: Statistical and Computational Methods for Scientists and Engineers, fourth ed. Springer International Publishing, Switzerland.

Breese, M.B.H., 1993. A theory of ion beam induced charge collection. J. Appl. Phys. 34, 3789–3799.

Breese, M.B.H., Vittone, E., Vizkelethy, G., Sellin, P.J., 2007. A review of ion beam induced charge microscopy. Nucl. Instrum. Methods Phys. Res. B 264, 345–360.

Brun, R., Couet, O., Vandoni, C.E., Zanarini, P., 1989. PAW, a general-purpose portable software tool for data analysis and presentation. Comput. Phys. Commun. 57, 432–437.

Bueno, C.C., Gonçalves, J.A.C., de, S., Santos, M.D., 1996. The performance of low-cost commercial photodiodes for charged particle and X-ray spectrometry. Nucl. Instrum. Methods Phys. Res. 371, 460–464.

Bueno, C.C., Gonçalves, J.A.C., Magalhães, R.R., Santos, M.D.S., 2004. Response of PIN diodes as room temperature photon detectors. Appl. Radiat. Isot. 61, 1343–1347.

Chaoui, Z., Azli, T., 2010. Dead-layer effect in silicon detectors: yield spectra of reflected electrons. Surf. Interface Anal. 42, 1089–1092.

Chaoui, Z., Ding, Z.J., Goto, K., 2009. Energy spectra of electron yields from silicon: theory and experiment. Phys. Lett. 373, 1679–1682.

Chaoui, Z., Goto, K., 2010. Auger electron from silicon: comparison of full Monte Carlo simulations with experiment. Surf. Interface Anal. 42, 1105–1108.

Chaoui, Z., Renschler, P., 2010. Dead layer effect in silicon detectors: energy deposited. Surf. Interface Anal. 42, 1093–1095.

Clifford, E.T.H., Hagberg, E., Koslowsy, V.T., Hardy, J.C., Schmeing, H., Azuma, R.E., 1984. Measurements of the response of a hybrid detector telescope to mono-energetic beams of positrons and electrons in the energy range 0.8–3.8 MeV. Nucl. Instrum. Methods 224, 440–447.

Cromer, D.T., Liberman, D., 1970. Relativistic Calculation of Anomalous Scattering Factors for X Rays. Los Alamos Scientific Laboratory report. LA-4403.

Damkjaer, A., 1982. The response of a silicon surface barrier detector to monoenergetic electrons in the range 100–600 keV. Nucl. Instrum. Methods 200, 377–381.

De Napoli, M., Giacoppo, F., Raciti, G., Rapisarda, E., 2009. Study of charge collection efficiency in 4H–SiC Schottky diodes with ^{12}C ions. Nucl. Instrum. Methods Phys. Res. 608, 80–85.

Decker, R., Wünsch, K.-D., Wollnik, H., Jung, G., Koglin, E., Siegert, G., 1982. A hyperpure Germanium detector for precise beta endpoint energy determinations. Nucl. Instrum. Methods 192, 261–272.

Fernández-Varea, J.M., Jahnke, V., Maidana, N.L., Malafronte, A.A., Vanin, V.R., 2014. Cross sections of K-shell ionization by electron impact, measured from threshold to 100 keV, for Au and Bi. J. Phys. B 47, 155201.

Fraser, G.W., Abbey, A.F., Holland, A., McCarthy, K., Owens, A., Wells, A., 1994. The x-ray energy response of silicon Part A. Theory. Nucl. Instrum. Methods Phys. Res. B 350, 368–378.

Frommhold, T., Arnold, W., Friedrichs, H., Göbel, R., Heil, R.D., Kneissl, U., Seemann, U., Steiper, F., Kozhuharov, C., 1991. Response functions of Si detectors to monoenergetic electrons and positrons in the energy range 0.8–3.5 MeV. Nucl. Instrum. Methods Phys. Res. 310, 657–664.

Gao, F., Campbell, L.W., Devanathan, R., Xie, Y., Corrales, L.R., Peurrung, A.J., Weber, W.J., 2007. Monte Carlo method for simulating γ-ray interaction with materials: a case study on Si. Nucl. Instrum. Methods Phys. Res. 579, 292–296.

Gooda, P.H., Gilboy, W.B., 1987. High resolution alpha spectroscopy with low cost photodiodes. Nucl. Instrum. Methods Phys. Res. 255, 222–224.

Goto, S., 1993. Response functions of a Si(Li) detector for photon energies from 1 to 10 keV. Nucl. Instrum. Methods Phys. Res. 333, 452–457.

Goto, S., 1998. Detailed simulation of the response function of an Si(Li) detector. J. Synchrotron Radiat. 5, 880–882.

Hartmann, R., Hauff, D., Lechner, P., Richter, R., Strüder, L., Kemmer, J., Krisch, S., Scholze, F., Ulm, G., 1996. Low energy response of silicon pn-junction detector. Nucl. Instrum. Methods Phys. Res. 377, 191–196.

He, T., Gardner, R.P., Verghese, K., 1990. An improved Si(Li) detector response function. Nucl. Instrum. Methods 299, 354–366.

Hollstein, M., 1970. Response characteristics of a high-resolution Si(Li) photon spectrometer. Nucl. Instrum. Methods 82, 249–252.

Iwamoto, N., Onoda, S., Makino, T., Ohshima, T., Kojima, K., Koizumi, A., Uchida, K., Nozaki, S., 2011. Transient analysis of an extended drift region in a 6H–SiC diode formed by a single particle strike and its contribution to the increased charge collection. IEEE Trans. Nucl. Sci. 58, 305–313.

Jablonski, A., Salvat, F., Powell, C.J., Lee, A.Y., 2016. NIST Electron Elastic-Scattering Cross-Section Database Version 4.0, NIST Standard Reference Database Number 64. National Institute of Standards and Technology, Gaithersburg MD, p. 20899. https://srdata.nist.gov/srd64/.

Jakšić, M., Medunić, Z., Bogovac, M., Skukan, N., 2005. Radiation damage microstructures in silicon and application in position sensitive charged particle detection. Nucl. Instrum. Methods Phys. Res. B 231, 502–506.

James, F., Roos, M., 1975. Minuit - a system for function minimization and analysis of the parameter errors and correlations. Comput. Phys. Commun. 10, 343–367.

Knoll, G.F., 2010. Radiation Detection and Measurement, fourth ed. Wiley, New York, USA.

Kojima, Y., Ikuta, T., Asai, M., Taniguchi, A., Shibata, M., Yamamoto, H., 1997. Measurement of response function of HPGe detectors for monoenergetic electrons and positrons in an energy range of 6.0–9.0 MeV. Nucl. Instrum. Methods Phys. Res. B 126, 419–422.

Llovet, X., Salvat, F., Bote, D., Salvat-Pujol, F., Jablonski, A., Powell, C.J., 2014. NIST Database of Cross Sections for Inner-Shell Ionization by Electron or Positron Impact, Version 1.0, NIST Standard Reference Database Number 164. National Institute of Standards and Technology, Gaithersburg MD, p. 20899. https://doi.org/10.18434/T4N881.

Malafronte, A.A., Petri, A.R., Gonçalves, J.A.C., Barros, S.F., Bueno, C.C., Maidana, N.L., Mangiarotti, A., Martins, M.N., Quivy, A.A., Vanin, V.R., 2020. A low-cost small-size commercial PIN photodiode: I. electrical characterisation and low-energy photon spectrometry. Radiat. Phys. Chem. https://doi.org/10.1016/j.radphyschem.2020.109103.

Manfredotti, C., Fizzotti, F., Lo Giudice, A., Paolini, C., Vittone, E., Nava, F., 2001. Investigation of 4H–SiC Schottky diodes by ion beam induced charge (IBIC) technique. Appl. Surf. Sci. 184, 448–454.

Otto, H., Peuser, P., Nyman, G., Roeckl, E., 1979. Determination of Q$_\beta$ values from endpoint energies of beta spectra. Nucl. Instrum. Methods Phys. Res. 166, 507–514.

Owens, A., 1985. Spectral degradation effects in an 86 cm^3 Ge(HP) detector. Nucl. Instrum. Methods Phys. Res. 238, 473–478.

Penn, D.R., 1987. Electron mean-free-path calculations using a model dielectric function. Phys. Rev. B 35, 482–486.

Perkins, S.T., Cullen, D.E., Chen, M.H., Rathkopf, J., Scofield, J., Hubbell, J., 1991. Tables and Graphs of Atomic Subshell and Relaxation Data Derived from the LLNL Evaluated Atomic Data Library (EADL), Z=1–100, 30. University of California Radiation Laboratory report UCRL-50400.

Planskoy, B., 1968. Electron scattering from silicon semi-conductor detectors. Nucl. Instrum. Methods 61, 285–295.

Press, W.H., Flannery, B.P., Teukolsky, S.A., Vetterling, W.T., 1992. Numerical Recipes in FORTRAN 77, the Art of Scientific Computing, second ed. Cambridge University Press, Cambridge, England.

Rehfield, D.M., Moore, R.B., 1978. A study of the beta-ray response function and performance of an intrinsic-Germanium detector mounted in a superconducting solenoid. Nucl. Instrum. Methods 157, 365–387.

Renschler, P., 2011. KESS - A New Monte Carlo Simulation Code for Low-Energy Electron Interactions in Silicon Detectors. Ph.D. thesis. KIT, Karlsruhe.

Salvat, F., 2015. The PENELOPE code system. Specific features and recent improvements. Ann. Nucl. Energy 82, 98–109.

Salvat, F., 2019. PENELOPE-2018, A Code System for Monte Carlo Simulation of Electron and Photon Transport. OECD Nuclear Energy Agency, Workshop Proceedings, Barcelona, Spain, 28 January – 1 February.

Salvat, F., Jablonski, A., Powell, C.J., 2005. Elsepa - Dirac partial-wave calculation of elastic scattering of electrons and positrons by atoms, positive ions and molecules. Comput. Phys. Commun. 165, 157–190.

Scholze, F., Procop, M., 2001. Measurement of detection efficiency and response functions for an Si(Li) x-ray spectrometer in the range 0.1–5 keV. X Ray Spectrom. 30, 69–76.

Schüpferling, H.M., 1975. Response functions of 4π Si(Li) semiconductor spectrometer for electrons. Nucl. Instrum. Methods 123, 67–71.

Sempau, J., Acosta, E., Baró, J., Fernández-Varea, J.M., Salvat, F., 1997. An algorithm for Monte Carlo simulation of coupled electron-photon transport. Nucl. Instrum. Methods Phys. Res. B 132, 377–390.

Sempau, J., Badal, A., Brualla, L., 2011. A PENELOPE-based system for the automated Monte Carlo simulation of clinacs and voxelized geometries-application to far-from-axis fields. Med. Phys. 38, 5887–5895.

Sempau, J., Fernández-Varea, J., Acosta, E., Salvat, F., 2003. Experimental benchmarks of the Monte Carlo code PENELOPE. Nucl. Instrum. Methods Phys. Res. B 207, 107–123.

Tabata, T., Ito, R., Okabe, S., 1971. An empirical equation for the backscattering coefficient of electrons. Nucl. Instrum. Methods Phys. Res. 94, 509–513.

Tsoulfanidis, N., Wehring, B.W., Wyman, M.E., 1969. The use of an analytical response function for unfolding beta spectra. Nucl. Instrum. Methods 73, 98–102.

Vanin, V.R., Manso Guevara, M.V., Maidana, N.L., Martins, M.N., Fernández-Varea, J., 2016. Ag K-shell ionization by electron impact: new cross-section measurements between 50 and 100 kev and review of previous experimental data. Radiat. Phys. Chem. 119, 14–23.

Vanin, V.R., Maidana, N.L., Mangiarotti, A., Lima, R.R., Malafronte, A.A., Barros, S.F., Martins, M.N., 2019. The 10–100 keV beam line of the São Paulo Microtron electron accelerator. Radiat. Phys. Chem. 154, 26–31.

Vittone, E., Fizzotti, F., Gargioni, E., Lu, R., Polesello, P., Lo Giudice, A., Manfredotti, C., Galassini, S., Jaksic, M., 1999. Evaluation of the diffusion length in silicon diodes by means of the lateral IBIC technique. Nucl. Instrum. Methods Phys. Res. B 158, 476–480.

Wall, B.L., Amsbaugh, J.F., Beglarian, A., Bergmann, T., Bichsel, H.C., Bodine, L.I., Boyd, N.M., Burritt, T.H., Chaoui, Z., Corona, T.J., Doe, P.J., Enomoto, S., Harms, F., Harper, G.C., Howe, M., Martin, E.L., Parno, D.S., Peterson, D., Petzold, L., Renschler, P., Robertson, R.G.H., Schwarz, J., Steidl, M., Van Wechel, T.D., Devender, B.A.V., Wüstling, S., Wierman, K.J., Wilkerson, J., 2014. Dead layer on silicon p–i–n diode charged-particle detectors. Nucl. Instrum. Methods Phys. Res. 744, 73–79.

Wall, B.L., Burritt, T.H., Doe, P.J., Fredericks, C., Gemmeke, H., Harper, G.C., Howe, M.A., Leber, M., Myers, A.W., Robertson, R.G.H., Steidl, M., VanDevender, B.A., Wechel, T.D.V., Wüstling, S., Wilkerson, J.F., 2006. Dead layer measurements for KATRIN prototype PIN diode array. IEEE Nucl Sci Symp Conf Rec 1, 204–207, 2006.

Weinheimer, C., Schrader, M., Bonn, J., Loeken, T., Backe, H., 1992. Measurement of energy resolution and dead layer thickness of LN^2-cooled PIN photodiodes. Nucl. Instrum. Methods Phys. Res. 311, 273–279.

Yamamoto, H., Hatakeyama, S., Norimura, T., Tsuchiya, T., 1988. Low energy nuclear radiation detection with a silicon photodiode. Nucl. Instrum. Methods Phys. Res. 281, 128–132.

Zevallos-Chávez, J.Y., da Cruz, M.T.F., Martins, M.N., Likhachev, V.P., Zamboni, C.B., Camargo, S., Genezini, F.A., Medeiros, J.A.G., Hindi, M.M., 2001. Response function of a germanium detector to photon energies between 6 and 120 keV. Nucl. Instrum. Methods Phys. Res. 457, 212–219.

Zhao, S., Gohil, T., Lioliou, G., Barnett, A.M., 2016. Soft X-ray detection and photon counting spectroscopy with commercial 4H-SiC Schottky photodiodes. Nucl. Instrum. Methods Phys. Res. 830, 1–5.